

NASA

TP
1749
c. 1

NASA Technical Paper 1749

LOAN COPY: R
AFWL TECHNICAL
KIRTLAND AFB

0067567



TECH LIBRARY KAFB, NM

Numerical Simulation of Steady Supersonic Viscous Flow

Lewis B. Schiff and Joseph L. Steger

MAY 1981





NASA Technical Paper 1749

Numerical Simulation of Steady Supersonic Viscous Flow

Lewis B. Schiff and Joseph L. Steger
Ames Research Center
Moffett Field, California



National Aeronautics
and Space Administration

**Scientific and Technical
Information Branch**

1981



NUMERICAL SIMULATION OF STEADY SUPERSONIC VISCOUS FLOW*

Lewis B. Schiff and Joseph L. Steger[†]

Ames Research Center

I. SUMMARY

A noniterative, implicit, space-marching, finite-difference algorithm is developed for the steady thin-layer Navier-Stokes equations in conservation-law form. The numerical algorithm is applicable to steady supersonic viscous flow over bodies of arbitrary shape. In addition, the same code can be used to compute supersonic inviscid flow or three-dimensional boundary layers. Computed results from two-dimensional and three-dimensional versions of the numerical algorithm are in good agreement with those obtained from more costly time-marching techniques.

II. INTRODUCTION

Considerable effort is being directed toward developing efficient finite-difference, numerical algorithms for the solution of the unsteady compressible Navier-Stokes equations. Although current algorithms are considerably more efficient than those available even a few years ago, the cost of time-marched Navier-Stokes solutions is not trivial. Furthermore, the computation of viscous flow about practical three-dimensional configurations is currently restricted by the size of available computer storage.

For steady, supersonic, high Reynolds number viscous flows about configurations with moderate axial-geometry variation, a substantial additional reduction in both computational effort and required storage can be achieved by utilizing the parabolized Navier-Stokes equations. The parabolized Navier-Stokes equations are obtained by (1) neglecting the unsteady terms as well as the streamwise viscous diffusion terms within the Navier-Stokes equations, and (2) by modifying the streamwise convective flux vector to permit stable time-like marching of the equations downstream from initial data. The resulting equations are commonly referred to as the parabolized Navier-Stokes equations because they are parabolic-like with respect to the downstream marching coordinate. Computational efficiency and reduced storage requirements are obtained because the parabolized equations are solved by advancing an initial plane of data in space, rather than by advancing an initial cube of data in time, as is done for the full Navier-Stokes equations. The parabolized

*Presented at 17th Aerospace Sciences Meeting, New Orleans, La., January 15-17, 1979.

[†]Present address: Dept. of Aeronautics and Astronautics, Stanford University, Stanford, Calif. 94305.

Navier-Stokes approximation has been employed by numerous researchers for both external flows (cf. refs. 1-6) and internal flows (cf. refs. 7-12). A variety of numerical algorithms has been used to advance the resulting equations and, as discussed in section III, many of these are unstable.

In this report, we present a noniterative, implicit, finite-difference algorithm, analogous to that developed by Beam and Warming (cf. refs. 13, 14) for unsteady flow, for the solution of the parabolized Navier-Stokes equations. The algorithm is conservative, second-order accurate in the marching direction, and can be second- or fourth-order accurate in the transverse directions. Although it was developed independently, our numerical algorithm is computationally similar to one recently reported by Vigneron, Rakich, and Tannehill (ref. 6), but it differs crucially in the treatment of the streamwise pressure gradient within the subsonic viscous layer.

In section III, we detail the governing equations, the parabolized Navier-Stokes approximation, and the numerical algorithm for steady two-dimensional flow. Section III also contains sample computed results and a discussion of the stability of the present method. In section IV, we outline the extension of the method to steady three-dimensional flow, and present sample results that demonstrate the accuracy and versatility of the resulting factored algorithm.

III. TWO-DIMENSIONAL FLOW

Discussion of the parabolized Navier-Stokes approximation and illustration of the numerical algorithm are facilitated if we first consider the case of steady two-dimensional flow. The extension to steady three-dimensional flow is given in section IV.

Governing Equations

Generalized coordinate transformation- To accommodate body-conforming coordinates, we introduce new independent spatial variables that transform the physical x, z plane surrounding the body (fig. 1(a)) into a rectangular ξ, ζ computational plane (fig. 1(b)). The transformation, of the form

$$\left. \begin{aligned} \xi &= \xi(x) = \text{streamwise coordinate} \\ \zeta &= \zeta(x, z) = \text{normal coordinate} \end{aligned} \right\} \quad (1)$$

maps the body surface onto $\zeta = 0$. This transformation both simplifies the application of surface boundary conditions, and makes possible the approximation of neglecting streamwise viscous terms in high Reynolds number flow. The Jacobian of the transformation is

$$J = \xi_x \zeta_z = \frac{1}{x_\xi z_\zeta} \quad (2)$$

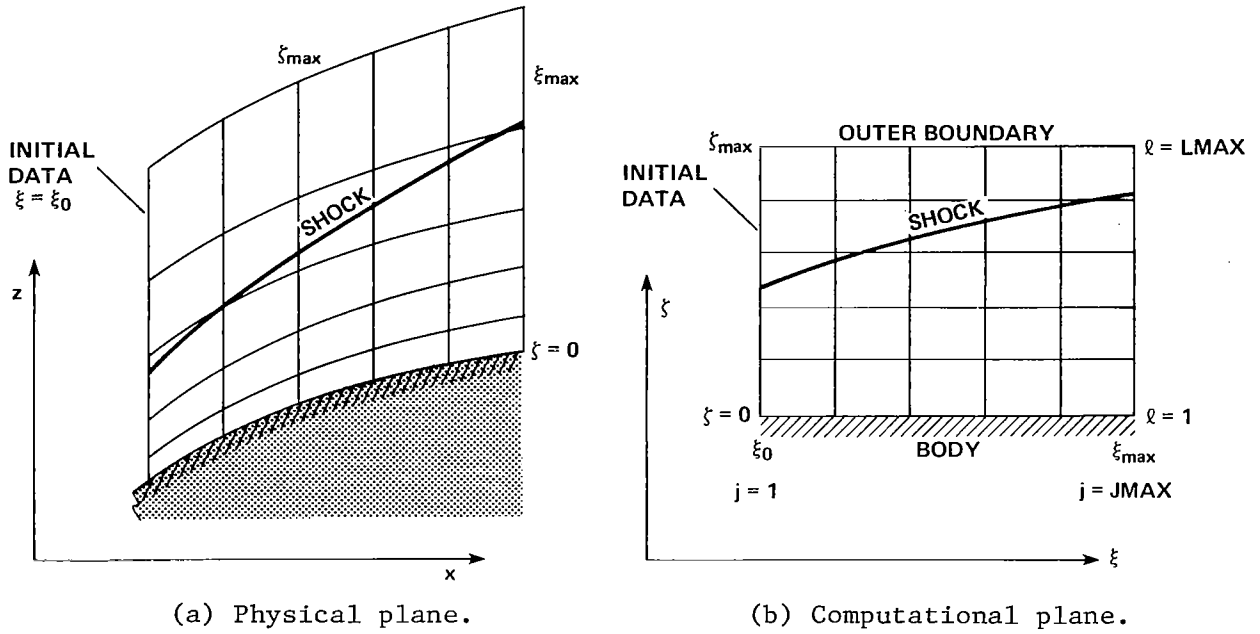


Figure 1.- Mapping of physical plane into computational plane.

and the metric derivatives ξ_x, ζ_x , etc., in the computational plane, are related to those in the physical plane, x_ξ, z_ξ , etc., by

$$\xi_x = Jz_\zeta \quad \xi_z = 0 \quad \zeta_x = -Jz_\xi \quad \zeta_z = Jx_\xi \quad (3)$$

In this report we consider ξ to be $\xi(x)$ only. Thus, vertical lines in the physical plane map into vertical lines of the computational plane.

Transformation of gasdynamic equations- The steady Navier-Stokes equations, written in strong conservation-law form for Cartesian spatial variables x, z , can be expressed in nondimensional variables as

$$\frac{\partial E}{\partial x} + \frac{\partial G}{\partial z} = \frac{1}{Re} \left(\frac{\partial R}{\partial x} + \frac{\partial S}{\partial z} \right) \quad (4)$$

where

$$E = E(q) = \begin{pmatrix} \rho u \\ \rho u^2 + p \\ \rho w u \\ (e + p)u \end{pmatrix}, \quad G = G(q) = \begin{pmatrix} \rho w \\ \rho u w \\ \rho w^2 + p \\ (e + p)w \end{pmatrix}, \quad q = \begin{pmatrix} \rho \\ \rho u \\ \rho w \\ e \end{pmatrix}$$

and the form of the viscous term is discussed in the section on *Viscous model* (p. 4).

The strong conservation-law form can be preserved under the ξ, ζ transformation of coordinates by retaining the Cartesian velocity components as dependent variables (cf. refs. 15, 16), and the transformed equation becomes

$$\frac{\partial \hat{E}}{\partial \xi} + \frac{\partial \hat{G}}{\partial \zeta} = \frac{1}{\text{Re}} \left(\frac{\partial \hat{R}}{\partial \xi} + \frac{\partial \hat{S}}{\partial \zeta} \right) \quad (5)$$

where

$$\hat{E} = \frac{\xi_x}{J} E = \frac{1}{J} \begin{pmatrix} \rho U \\ \rho u U + \xi_x p \\ \rho w U \\ (e + p) U \end{pmatrix}, \quad \hat{q} = \frac{1}{J} q = \frac{1}{J} \begin{pmatrix} \rho \\ \rho u \\ \rho w \\ e \end{pmatrix},$$

$$\hat{G} = \frac{\zeta_x}{J} E + \frac{\zeta_z}{J} G = \frac{1}{J} \begin{pmatrix} \rho W \\ \rho u W + \zeta_x p \\ \rho w W + \zeta_z p \\ (e + p) W \end{pmatrix}$$

and the contravariant velocity components U, W are defined in terms of the Cartesian velocity components u, w as

$$\left. \begin{aligned} U &= \xi_x u \\ W &= \zeta_x u + \zeta_z w \end{aligned} \right\} \quad (6)$$

The internal energy of the gas, e_i , is defined in terms of the conservative variables as

$$e_i = \frac{e}{\rho} - 0.5(u^2 + w^2) \quad (7)$$

and for a perfect gas with ratio of specific heats γ , the equation of state is

$$\frac{p}{\rho} = (\gamma - 1)e_i = \frac{a^2}{\gamma}$$

In equations (4)-(7) the Cartesian velocity components u, w are made non-dimensional with respect to a_∞ (the free-stream speed of sound), density ρ is normalized by ρ_∞ , and total energy e is referenced to $\rho_\infty a_\infty^2$.

Viscous model- The first step in obtaining the parabolized Navier-Stokes equations from equation (5) is to neglect all streamwise derivatives, $\partial/\partial \xi$, within the viscous terms. This approximation is physically justified for high

Reynolds number flow past body-conforming coordinates by using the usual arguments of boundary-layer theory (see also ref. 17 or 18 for related hypersonic viscous-flow analysis). Neglect of the streamwise viscous terms is necessary to prevent exponential growth in marching the equations in ξ , that is, to mathematically change the nature of equation (5) from elliptic to parabolic type with respect to the ξ coordinate. On neglecting the streamwise derivatives, equation (5) can be written as

$$\frac{\partial \hat{E}}{\partial \xi} + \frac{\partial \hat{G}}{\partial \zeta} = \frac{1}{\text{Re}} \frac{\partial \hat{S}}{\partial \zeta} \quad (8)$$

where, in equation (8)

$$\hat{S} = \frac{1}{J} \begin{pmatrix} 0 \\ \mu(\zeta_x^2 + \zeta_z^2)u_\zeta + (\mu/3)(\zeta_x u_\zeta + \zeta_z w_\zeta)\zeta_x \\ \mu(\zeta_x^2 + \zeta_z^2)w_\zeta + (\mu/3)(\zeta_x u_\zeta + \zeta_z w_\zeta)\zeta_z \\ (\zeta_x^2 + \zeta_z^2)[(\mu/2)(u^2 + w^2)_\zeta + \kappa \text{Pr}^{-1}(\gamma - 1)^{-1}(a^2)_\zeta] \\ + (\mu/3)(\zeta_x u + \zeta_z w)(\zeta_x u_\zeta + \zeta_z w_\zeta) \end{pmatrix} \quad (9)$$

In obtaining equation (9), use has been made of the Stokes hypothesis, $\lambda = -2\mu/3$, where λ and μ are the coefficients of viscosity. Also, κ is the coefficient of thermal conductivity, Re is the free-stream Reynolds number, and Pr is the free-stream Prandtl number. For turbulent flow computations the eddy-viscosity model described by Baldwin and Lomax (ref. 19) is employed.

Boundary conditions- Surface boundary conditions for equation (8) are simplified because the body surface has been mapped onto $\zeta = 0$ (see fig. 1). The steady no-slip condition is simply given by $U = W = 0$. The pressure on the body surface can be determined from the ζ momentum equation, evaluated at the wall, which becomes

$$\frac{\partial}{\partial \zeta} \left(\frac{\zeta_z}{J} p \right) = \frac{1}{\text{Re}} \frac{\partial}{\partial \zeta} \left(\frac{\zeta_x^2 + (4/3)\zeta_z^2}{J} \mu w_\zeta + \frac{\zeta_x \zeta_z}{J} \frac{\mu}{3} u_\zeta \right)$$

However, a simplified boundary condition, $\partial p / \partial \zeta = 0$, is consistent with restrictions to be placed on the governing equations to maintain a stable streamwise marching procedure. The surface density is obtained from the equation of state using the found surface pressure and a specification of either the wall temperature or temperature gradient.

In the present computations no provision has been made for fitting the bow shock wave. Instead, the outer edge of the computational region, $\zeta = \zeta_{\text{max}}$, is chosen to extend into the undisturbed free stream beyond the shock layer, and the bow shock is captured.

A solution consistent with the parabolized Navier-Stokes approximation must be supplied as initial data. The initial data must be those of supersonic

external flow, and the streamwise component of velocity must be everywhere positive.

Jacobian matrices of the flux vectors- Jacobian matrices of the flux vectors are needed in our development of both the parabolized Navier-Stokes equations and in the implicit marching algorithm to be described later. Since the flux vectors \hat{E} and \hat{G} are linear combinations of the Cartesian flux vectors E and G ,

$$\hat{E} = \frac{\xi_x}{J} E, \quad \hat{G} = \frac{\zeta_x}{J} E + \frac{\zeta_z}{J} G \quad (10)$$

the Jacobian matrices $\hat{A} \equiv [\partial\hat{E}/\partial\hat{q}]$ and $\hat{C} \equiv [\partial\hat{G}/\partial\hat{q}]$ can be written as

$$\hat{A} = \xi_x A, \quad \hat{C} = \zeta_x A + \zeta_z C \quad (11)$$

in terms of the Jacobian matrices of the Cartesian flux vectors $A \equiv [\partial E/\partial q]$ and $C \equiv [\partial G/\partial q]$. Any one matrix can be obtained from the general form

$$\hat{A} \text{ or } \hat{C} = \begin{bmatrix} 0 & K_1 & K_2 & 0 \\ K_1\phi^2 - u\theta & \theta - K_1(\gamma - 2)u & K_2u - (\gamma - 1)K_1w & K_1(\gamma - 1) \\ K_2\phi^2 - w\theta & K_1w - K_2(\gamma - 1)u & \theta - K_2(\gamma - 2)w & K_2(\gamma - 1) \\ \theta[2\phi^2 - \gamma(e/\rho)] & \{K_1[\gamma(e/\rho) - \phi^2] \\ & - (\gamma - 1)u\theta\} & \{K_2[\gamma(e/\rho) - \phi^2] \\ & - (\gamma - 1)w\theta\} & \gamma\theta \end{bmatrix} \quad (12)$$

where

$$\phi^2 = 0.5(\gamma - 1)(u^2 + w^2), \quad \theta = K_1u + K_2w$$

To obtain the matrix \hat{A} , set $K_1 = \xi_x$ and $K_2 = 0$, and to obtain the Jacobian matrix \hat{C} , set $K_1 = \zeta_x$ and $K_2 = \zeta_z$. The Cartesian Jacobian matrices A and C are obtained from equation (12) with $K_1 = 1$, $K_2 = 0$, and with $K_1 = 0$, $K_2 = 1$, respectively.

The Cartesian flux vectors E and G are homogeneous functions of degree one in q . As a consequence, they possess the identities

$$E = Aq \quad G = Cq \quad (13)$$

The homogeneous property also extends to the generalized flux vectors, that is,

$$\hat{E} = \hat{A}\hat{q} \quad \hat{G} = \hat{C}\hat{q} \quad (14)$$

With the streamwise variation of the coefficients of viscosity μ and thermal conductivity κ neglected, a Jacobian matrix operator for the viscous term can be written as

$$\hat{M} = \frac{1}{J} \begin{bmatrix} 0 & 0 & 0 & 0 \\ m_{21} & \alpha_1 \partial_\zeta (1/\hat{\rho}) & \alpha_2 \partial_\zeta (1/\hat{\rho}) & 0 \\ m_{31} & \alpha_2 \partial_\zeta (1/\hat{\rho}) & \alpha_3 \partial_\zeta (1/\hat{\rho}) & 0 \\ m_{41} & m_{42} & m_{43} & \alpha_4 \partial_\zeta (1/\hat{\rho}) \end{bmatrix} \quad (15)$$

with

$$m_{21} = -\alpha_1 \partial_\zeta (u/\hat{\rho}) - \alpha_2 \partial_\zeta (w/\hat{\rho})$$

$$m_{31} = -\alpha_2 \partial_\zeta (u/\hat{\rho}) - \alpha_3 \partial_\zeta (w/\hat{\rho})$$

$$m_{41} = \alpha_4 \partial_\zeta [-(\hat{e}/\hat{\rho}^2) + (u^2 + w^2)/\hat{\rho}] - \alpha_1 \partial_\zeta (u^2/\hat{\rho}) - 2\alpha_2 \partial_\zeta (uw/\hat{\rho}) - \alpha_3 \partial_\zeta (w^2/\hat{\rho})$$

$$m_{42} = -\alpha_4 \partial_\zeta (u/\hat{\rho}) - m_{21}$$

$$m_{43} = -\alpha_4 \partial_\zeta (w/\hat{\rho}) - m_{31}$$

$$\alpha_1 = \mu [(4/3)\zeta_x^2 + \zeta_z^2] , \quad \alpha_2 = (\mu/3)\zeta_x \zeta_x$$

$$\alpha_3 = \mu [\zeta_x^2 + (4/3)\zeta_z^2] , \quad \alpha_4 = (\gamma\kappa/\text{Pr})(\zeta_x^2 + \zeta_z^2)$$

and

$$\hat{\rho} = (\rho/J) \quad \hat{e} = (e/J)$$

The viscous term is homogeneous of degree zero in \hat{q} and thus possesses the property that

$$\hat{M}\hat{q} = 0 \quad (16)$$

The Parabolized Navier-Stokes Approximation

Conditions for stable marching- As alluded to in the introduction, the parabolized Navier-Stokes approximation for steady supersonic external flow employs two main assumptions: (1) the viscous terms in the marching direction ξ (which we loosely refer to as streamwise) are negligible, and (2) the streamwise convective flux derivative has positive time-like behavior (discussed below) with respect to the remaining spatial derivatives. The first approximation is justified for high Reynolds number flow and body-conforming coordinates and has been discussed above. The second assumption is the most difficult restriction to impose on the parabolized Navier-Stokes equations. With the Navier-Stokes equations arranged as in equation (8), by positive time-like behavior in ξ , we mean that the Jacobian matrix A has positive eigenvalues. Although we oversimplify, the restriction that A has positive eigenvalues is required in inviscid flow for the equations to be hyperbolic and it is needed in viscous flow if positive viscosity is to cause damping in

the marching direction. Insofar as the viscous flow near a no-slip wall is subsonic, at least one eigenvalue of A , the $u - a$ root, will be less than zero. Consequently, the solution can grow exponentially with marching unless this negative root is suppressed.

This becomes readily apparent if we consider a linearized frozen (i.e., locally constant) coefficient form of equation (8).

$$\hat{A}_f \frac{\partial \hat{q}}{\partial \xi} + \hat{C}_f \frac{\partial \hat{q}}{\partial \zeta} = \frac{1}{\text{Re}} \hat{N}_f \frac{\partial^2 \hat{q}}{\partial \zeta^2} + f_o \quad (17)$$

where \hat{A}_f , \hat{C}_f , and \hat{N}_f are constant coefficient matrices with elements defined by equations (12) and (15). The matrix \hat{N}_f differs from \hat{M} insofar as the operators $\partial/\partial \zeta$ have been shifted to the right. To the lowest order linearization $f_o = 0$, otherwise f_o is a known function and contains linearization terms such as $\text{Re}^{-1} \partial_\zeta (\hat{S}_o - \hat{N}_f \partial_\zeta \hat{q}_o)$, which result from the expansions $\hat{S} = \hat{S}_o + \hat{M}_o (\hat{q} - \hat{q}_o)$, $\hat{M}_o = \hat{N}_f \delta \zeta + \hat{\epsilon}$. The metrics are also assumed to be constant (i.e., uniform grid) as are the coefficients of viscosity and thermal conductivity.

If $u \neq a$ and $u \neq 0$, \hat{A}_f^{-1} exists and equation (17) can be rewritten as

$$\frac{\partial \hat{q}}{\partial \xi} + \hat{A}_f^{-1} \hat{C}_f \frac{\partial \hat{q}}{\partial \zeta} = \frac{1}{\text{Re}} \hat{A}_f^{-1} \hat{N}_f \frac{\partial^2 \hat{q}}{\partial \zeta^2} + \hat{A}_f^{-1} f_o \quad (18)$$

The eigenvalues of $\hat{A}_f^{-1} \hat{C}_f$ are $(1/\xi_x) \{ \zeta_x + \zeta_z [w/u, w/u, (uw \pm a\sqrt{u^2 + w^2 - a^2})/(u^2 - a^2)] \}$. The eigenvalues of $\hat{A}_f^{-1} \hat{N}_f$, computed with the simplification $\zeta_x = 0$, are given by

$$\sigma(\hat{A}_f^{-1} \hat{N}_f) = \frac{\zeta_z^2}{\xi_x} \left(0, \frac{4}{3} \frac{\mu}{\rho u}, \sigma_3, \sigma_4 \right) \quad (19)$$

where

$$\sigma_{3,4} = \frac{\mu}{2\rho(u^2 - a^2)} \left\{ \left(u + \frac{\gamma u^2 - a^2}{u P_r \mu / \kappa} \right) \pm \left[\left(u + \frac{\gamma u^2 - a^2}{u P_r \mu / \kappa} \right)^2 - \frac{4\gamma(u^2 - a^2)}{P_r \mu / \kappa} \right]^{1/2} \right\}$$

By introduction of a suitable similarity transform, either matrix product $\hat{A}_f^{-1} \hat{C}_f$ or $\hat{A}_f^{-1} \hat{N}_f$ can be diagonalized, but they cannot be simultaneously diagonalized. In particular, if X is the matrix whose column vectors are the independent eigenvectors of $\hat{A}_f^{-1} \hat{N}_f$, then introduction of

$$X^{-1} \hat{r} = \hat{q} \quad (20)$$

into equation (18) yields, on premultiplication by X ,

$$\frac{\partial \hat{r}}{\partial \xi} + X \hat{A}_f^{-1} \hat{C}_f X^{-1} \frac{\partial \hat{r}}{\partial \zeta} = \frac{1}{\text{Re}} \hat{D}_\sigma \frac{\partial^2 \hat{r}}{\partial \zeta^2} + g_o \quad (21)$$

where \hat{D}_G is a diagonal matrix with elements equal to the eigenvalues given by equation (19). If $0 < u < a$, $\hat{A}_F^{-1}\hat{N}_F$ has one negative real eigenvalue and the remaining eigenvalues are positive. This is evident from equation (19) where $\sigma_2 > 0$ if $u > 0$ and the roots $\sigma_{3,4} \propto \beta \pm \sqrt{\beta^2 - \theta(u^2 - a^2)}$ where $\theta = 4\gamma\kappa/\mu P_T > 0$. If $u < a$, $\sqrt{\beta^2 + \theta(a^2 - u^2)} > \beta$ so one root must be positive real and one root must be negative real. Which of the roots σ_3 or σ_4 is negative depends on the magnitude of u .

Taking σ_4 as the negative root for $u < a$, the fourth scalar equation of equation (21) is seen to have an effective negative viscosity. As such, the fourth vector component \hat{r}_4 grows exponentially with marching in ξ . Moreover, even if the diffusion coefficient is negligible, the roots of $\hat{A}_F^{-1}\hat{C}_F$ are complex if $u^2 + w^2 \leq a^2$. Thus, the inviscid part is not hyperbolic in ξ unless $u^2 + w^2 > a^2$. Consequently, for stable streamwise marching, the eigenvalues of $\hat{A}_F^{-1}\hat{N}_F$ must be positive real while the roots of $\hat{A}_F^{-1}\hat{C}_F$ should be real. Although stated as an oversimplification of the matrix algebra, these conditions occur precisely when \hat{A}_F has positive real roots.

The subsonic layer model- Two observations are now made. The first is that if pressure can be specified in the flux vector E , that is, the given p is not a function of q , then the sound speed contribution to the eigenvalues of $[\partial E/\partial q] = A$ is removed. In this way, the eigenvalues of A remain positive as long as $u > 0$. The second observation is that, for high Reynolds number viscous flow, pressure is approximately constant through the thin subsonic viscous sublayer near the wall. Indeed, according to boundary-layer theory, for high Reynolds number flow the approximation $\partial p/\partial n = 0$ is valid over the entire thickness of the viscous layer. Thus, this approximation is even more apropos over just the subsonic portion of the viscous layer.

Although developed under a different formalism, these observations form the basis of the parabolized Navier-Stokes approximation that Rubin and Lin (cf. refs. 2, 3) term the sublayer approximation. In our development of the subsonic layer (i.e., sublayer) approximation, we begin by defining a new streamwise flux vector, \hat{E}_S , given by

$$\hat{E}_S = \frac{\xi_x}{J} E_S = \frac{\xi_x}{J} \begin{pmatrix} \rho u \\ \rho u^2 + p_S \\ \rho u w \\ u(e + p_S) \end{pmatrix} \quad (22)$$

where $p_S = (\gamma - 1)[e - 0.5\rho(u^2 + w^2)]$ for supersonic flow $u > a(1 + \epsilon_S)$ and p_S is defined from $\partial p/\partial \zeta = 0$ for subsonic flow $u < a(1 + \epsilon_S)$. Here we assume that ζ is effectively normal to the surface, and ϵ_S is a small positive number picked so that $u \neq a$ and A^{-1} exists.

A schematic of how p_S is evaluated is given in figure 2. The essential idea is that for points within the subsonic viscous sublayer p_S is not evaluated from the local flow variables but is taken from the adjacent

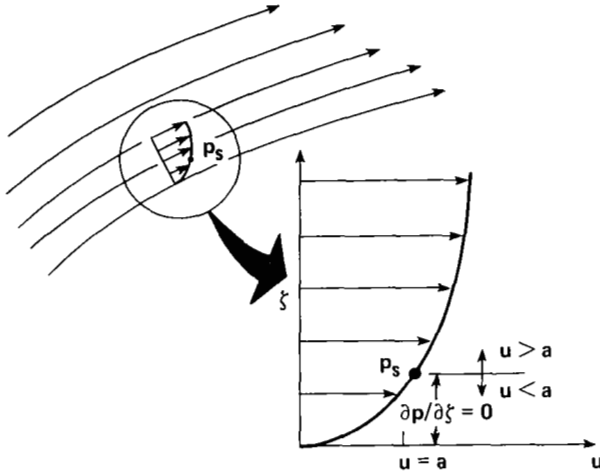


Figure 2.- Schematic of sublayer approximation showing p_s impressed from above.

supersonic flow. Throughout the subsonic sublayer it is assumed that $p_s \neq p_s(q)$, where q is the local vector of dependent variables. Of course, p_s is related to q in the adjacent supersonic region.

The Jacobian matrix, $A_u \equiv [\partial E_s / \partial q]$ where p_s is specified, has positive real roots if $u > 0$. By repeating the frozen coefficient analysis, it is shown below that equation (8) should be stable for marching in ξ if E is replaced by E_s . The Jacobian matrix A_u is given by

$$A_u = \begin{bmatrix} 0 & 1 & 0 & 0 \\ -u^2 & 2u & 0 & 0 \\ -uw & w & u & 0 \\ -u(e + p_s)/\rho & (e + p_s)/\rho & 0 & u \end{bmatrix} \quad (23)$$

and has eigenvalues $\sigma(A_u) = u, u, u, u$. Indeed, the vector E_s was originally constructed from similarity transforms so that A_u has the eigenvalues of u (see ref. 20 for related work).

The eigenvalues of $\hat{A}_u^{-1} \hat{N}_f$ ($\hat{A}_u \equiv \xi_x A_u$) with $\zeta_x = 0$, that is

$$\sigma(\hat{A}_u^{-1} \hat{N}_f) = \frac{\mu \zeta_z^2}{\rho u \xi_x} \left(0, 1, \frac{4}{3}, \frac{\gamma \kappa}{\mu \text{Pr}} \right) \quad (24)$$

are positive real if $u > 0$. Consequently, according to the frozen coefficient analysis, the viscous part of the initial value problem is stable for marching in ξ . We now examine the inviscid part of the equations. If for analysis purposes we apply the subsonic sublayer approximation to \hat{G} , then \hat{C}_u is defined and all four eigenvalues of $\hat{A}_u^{-1} \hat{C}_u$ are real, are identical, and are given by $(1/\xi_x)[\zeta_x + \zeta_z(w/u)]$. If the sublayer approximation is not imposed on \hat{G} , then under the restriction $\zeta_x = 0$, we find the eigenvalues of $\hat{A}_u^{-1} \zeta_z C$ are

$$\sigma(\hat{A}_u^{-1} \zeta_z C) = \frac{\zeta_z}{\xi_x} \left[\frac{w}{u}, \frac{w}{u}, \frac{w \pm a}{u} \right] \quad (25)$$

In either case the inviscid flow has real eigenvalues; however, the inviscid portion of the parabolized Navier-Stokes equations is not strictly hyperbolic because $\hat{A}_u^{-1} \hat{C}_u$ and $\hat{A}_u^{-1} C$ are defective by one eigenvector (as is A_u ; see, e.g., ref. 21 for a definition of hyperbolicity for first-order systems of equations). Apparently the inviscid part still retains a weak hyperbolicity. Curiously, the defective matrices A_u and C_u have eigenvalue properties like

those of simple commuting matrices, such as $\sigma(A_U)\sigma(C_U) = \sigma(A_U C_U)$ and $\sigma(A_U) + \sigma(C_U) = \sigma(A_U + C_U)$ (note that $A_U q = uq$).

Summarizing, the parabolized Navier-Stokes equations with the sublayer approximation can be expressed as

$$\frac{\partial \hat{E}_S}{\partial \xi} + \frac{\partial \hat{G}}{\partial \zeta} = \frac{1}{Re} \frac{\partial \hat{S}}{\partial \zeta} \quad (26)$$

where \hat{E}_S is defined by equation (22), and the equations are stable for marching in ξ when $u > 0$.

Relation to other work- Since the parabolized Navier-Stokes equations have been used extensively, we feel that it is important to show how equation (26) is related to past work. Although usually investigated without the eigenvalue formalism, it has long been recognized (cf. refs. 2, 3, 6, 7) that the crucial approximation in all parabolized Navier-Stokes schemes is in the treatment of the p_ξ (i.e., $\partial p / \partial \xi$) term in subsonic flow regions. In our development we think in terms of the pressure itself, but specifying p_S as a function of ξ is equivalent to specifying p_ξ .

The earliest successful parabolized Navier-Stokes schemes used the approximation that $p_\xi = 0$ in subsonic regions. This method always proved to be stable, as indeed it should be. According to the frozen coefficient theory, the marching should be stable when p_ξ is specified in subsonic regions and $u > 0$. Setting $p_\xi = 0$ in subsonic regions is equivalent to setting p_S to a specified constant, namely, the initial value of p_S .

Various researchers (refs. 1-6) have attempted to retain p_ξ in the subsonic regions. The usual idea has been to lag the differencing of p_ξ so as to treat it as a "source term." This, in fact, simply amounts to an explicit differencing of p_ξ . According to the frozen coefficient analysis, however, retaining p_ξ will always lead to instability in the limit of refined grid spacing. This occurs because the differential equations themselves admit exponential growth in the subsonic region unless the functional dependence of p_ξ is suppressed. Stability analysis by Lubard and Helliwell (ref. 5) seems to suggest that explicit differencing of p_ξ can lead to weaker instability than implicit differencing of p_ξ .

Any scheme that retains p_ξ in the subsonic sublayer relies on numerical dissipation to suppress unstable exponential growth. If the numerical scheme is consistent with the differential equations, then according to frozen coefficient analysis it will always be unstable as the grid spacing is refined.

A clever means of using numerical dissipation to control unstable growth due to retaining p_ξ has been employed by Lubard and Helliwell (ref. 5). As we interpret their technique, they take advantage of the fact that the implicit Euler numerical differencing scheme for initial-value problems will be stable in regions where the differential equation itself is unstable (see ref. 22 or 23 for the numerical stability bounds on the implicit Euler scheme). If the chosen step size is sufficiently large in Δx to suppress

the "physical" instability, but not so large as to trigger "nonlinear" instability, the Lubard and Helliwell scheme can be used to compute solutions. However, the method is always inconsistent in the sense that the grid spacing cannot be arbitrarily refined.

If the Lubard and Helliwell approach seems impractical, it must be remarked that the sublayer method also exhibits erratic divergence as the grid spacing in Δx is refined. So-called departure solutions are discussed in the literature (refs. 2, 3, 6). This behavior and a practical means of control will be discussed in the section on Departure Solutions and Global Iteration (p. 20). We simply comment here that the sublayer analysis previously discussed is a local analysis that does not account for global interaction between p_s and q of the outer flow.

More recently Vigneron, Rakich, and Tannehill (ref. 6) developed a parabolized Navier-Stokes scheme similar to the one developed in this paper. The crucial difference is that in reference 6 the authors attempted to approximate the p_ξ term with a weighting between implicit and explicit differencing that depends on the local Mach number.

Finally, we should note that a variety of parabolized Navier-Stokes schemes has been advanced for subsonic internal flow (refs. 7-12). The Patankar and Spalding (ref. 7) method appears to be the forerunner of these techniques and, as in the sublayer method, Patankar and Spalding determined p_ξ from special contrived relations based on the known mass flux through the channel.

Development of the Numerical Algorithm

A fully implicit, noniterative, finite-difference algorithm is constructed for the parabolized Navier-Stokes equations with the sublayer approximation. The difference equations are treated in vector form and their solution requires a block tridiagonal inversion at each marching step. Figure 1 indicates the extent of the computational domain and the definition of the indices j and ℓ .

Difference operators- An implicit, finite-difference scheme for equation (26) is constructed by selecting difference operators that would be stable for a model problem of diffusion and convection. The following difference approximations are selected for the inviscid flux vectors

$$\left(\frac{\partial \hat{E}_s}{\partial \xi}\right)^{j+1} \approx \frac{(\hat{E}_s^{j+1} - \hat{E}_s^j) - \alpha(\hat{E}_s^j - \hat{E}_s^{j-1})}{(1 - \alpha)\Delta\xi} + O(\Delta\xi)^{1+3\alpha} \quad (27)$$

where $\alpha = 0$ or $1/3$ for first- or second-order accuracy, and

$$\frac{\partial \hat{G}}{\partial \zeta} \approx \delta_\zeta \hat{G} = \frac{\hat{G}_{\ell+1} - \hat{G}_{\ell-1}}{2\Delta\zeta}, \quad O(\Delta\zeta)^2 \quad (28)$$

Each term of the viscous flux vector, $\partial_\zeta \hat{S}$, is of the form $\partial_\zeta(\phi \partial_\zeta \psi)$ and is differenced as

$$\bar{\delta}_\zeta \phi \bar{\delta}_\zeta \psi = \frac{(\phi_{\ell+1} + \phi_\ell)(\psi_{\ell+1} - \psi_\ell) - (\phi_\ell + \phi_{\ell-1})(\psi_\ell - \psi_{\ell-1})}{2\Delta\zeta^2} \quad (29)$$

Applying these operators to equation (26) gives

$$\frac{(\hat{E}_S^{j+1} - \hat{E}_S^j) - \alpha(\hat{E}_S^j - \hat{E}_S^{j-1})}{(1 - \alpha)\Delta\xi} + \left(\delta_\zeta \hat{G}^{j+1} - \frac{1}{\text{Re}} \bar{\delta}_\zeta \hat{S}^{j+1} \right) = 0 \quad (30)$$

This choice of difference operators is unconditionally stable for the model initial-value problem in ξ

$$\frac{\partial u}{\partial \xi} \pm \frac{\partial u}{\partial \zeta} = \frac{\partial^2 u}{\partial \zeta^2} \quad (31)$$

Because A or A_u has positive real roots, we expect the difference equations represented by equation (30) to be unconditionally linear stable.

Local linearizations- To avoid solving a nonlinear system of equations at each step in ξ , the flux vectors of equation (30) at $j+1$ are replaced by local linearizations about j . The local linearizations are defined as

$$E^{j+1} \approx E^j + A^j(q^{j+1} - q^j) = A^j q^{j+1} \quad (32a)$$

$$G^{j+1} \approx G^j + C^j(q^{j+1} - q^j) = C^j q^{j+1} \quad (32b)$$

$$\hat{G}^{j+1} \approx (\zeta_x^{j+1} A^j + \zeta_z^{j+1} C^j) \hat{q}^{j+1} \equiv \tilde{C}^j \hat{q}^{j+1} \quad (33a)$$

$$\hat{S}^{j+1} \approx \tilde{S}^j + \tilde{M}^j(\hat{q}^{j+1} - \hat{q}^j) = \tilde{S}^j + \tilde{M}^j \hat{q}^{j+1} \quad (33b)$$

where all of the approximations are $O(\Delta\xi)^2$ and we have used the homogeneous property, equation (13). The Jacobian matrices A , C , and M are defined by equations (12) and (15). Note that \sim indicates that the matrices \tilde{C}^j , \tilde{M}^j , and the vector \tilde{S}^j are evaluated using variables \hat{q} at j and metric quantities at $j+1$ (cf. eq. (33a)).

The special flux vector E_S , $u < a$, has the functional form $E_S = E_S(q, p_S)$ and locally linearizes as

$$E_S^{j+1} \approx E_S^j + \left[\frac{\partial E_S}{\partial q} \right]^j (q^{j+1} - q^j) + \left(\frac{\partial E_S}{\partial p_S} \right)^j (p_S^{j+1} - p_S^j) = A_u^j q^{j+1} + p_S^{j+1} \mathcal{P}^j \quad (34)$$

where A_u is previously defined (eq. (23)) while \mathcal{P} is the vector $\mathcal{P} = (0, 1, 0, u)^t$. The quantity p_S^{j+1} is also unknown, so we extrapolate

$$p_S^{j+1} = p_S^j + \beta(p_S^j - p_S^{j-1}) + O(\Delta\xi)^{1+\beta} \quad (35)$$

where $\beta = 0$ or 1 for first- or second-order accurate extrapolation. We remark that we have only exercised the $\beta = 0$ option because the error of the first-order approximation, confined to the thin sublayer, has not been significant in our test calculations.

The linearization of \hat{E}_s^{j+1} for either supersonic or subsonic flow can thus be expressed as

$$\hat{E}_s^{j+1} = \tilde{A}_s^j \hat{q}^{j+1} + \left(\frac{\xi_x}{J}\right)^{j+1} E_p^j \quad (36)$$

where

$$\tilde{A}_s^j = \tilde{A}^j = \xi_x^{j+1} A^j, \quad E_p^j = 0$$

in supersonic regions, $u > a$, and

$$\tilde{A}_s^j = \tilde{A}_u^j \equiv \xi_x^{j+1} A_u^j, \quad E_p^j = [p_s^j + \beta(p_s^j - p_s^{j-1})] \rho^j$$

in subsonic regions, $u < a$.

If only \hat{E}_s^{j+1} is locally linearized, the three-point backward difference operator becomes first order and nonconservative. That is, for $\alpha = 1/3$

$$\partial_{\xi} \hat{E}_s^{j+1} \approx \frac{[\tilde{A}_s^j \hat{q}^{j+1} + (\xi_x/J)^{j+1} E_p^j + 0(\Delta\xi)^2 - \hat{E}_s^j] - \alpha(\hat{E}_s^j - \hat{E}_s^{j-1})}{(1 - \alpha)\Delta\xi} \quad (37)$$

is $0(\Delta\xi)^2 / [(1 - \alpha)(\Delta\xi)] = 0(\Delta\xi)$ and is nonconservative. However, if \hat{E}_s^j is also linearized, the lowest-order linearization error will be subtracted off, that is,

$$\partial_{\xi} \hat{E}_s^{j+1} \approx \frac{[\tilde{A}_s^j \hat{q}^{j+1} + (\xi_x/J)^{j+1} E_p^j + 0(\Delta\xi)^2 - \tilde{A}_s^{j-1} \hat{q}^j - (\xi_x/J)^j E_p^{j-1} - 0(\Delta\xi)^2] - \alpha(\hat{E}_s^j - \hat{E}_s^{j-1})}{(1 - \alpha)\Delta\xi} \quad (38)$$

The difference approximation, equation (38), is $0(\Delta\xi)^2$ and is a conservative operator. Even if only first-order accuracy is required in ξ , $\alpha = 0$ above, it is still necessary to linearize each term of the difference $\hat{E}_s^{j+1} - \hat{E}_s^j$ to maintain a conservative differencing for shock-capturing purposes.

Delta form algorithm- Applying the local linearizations and adding a fourth-order dissipation term to equation (30) results in

$$\begin{aligned}
& (\tilde{A}_s^j \hat{q}^{j+1} - \tilde{A}_s^{j-1} \hat{q}^j) + (1 - \alpha) \Delta \xi (\delta_\zeta \tilde{C}^j - \text{Re}^{-1} \bar{\delta}_\zeta \tilde{M}^j) \hat{q}^{j+1} \\
& = (1 - \alpha) \Delta \xi \text{Re}^{-1} \bar{\delta}_\zeta \tilde{S}^j + \alpha (\hat{E}_s^j - \hat{E}_s^{j-1}) - [(\xi_x/J)^{j+1} E_p^j - (\xi_x/J)^j E_p^{j-1}] + \mathcal{O} \hat{q}^j
\end{aligned} \tag{39}$$

The fourth-order dissipation term has the form

$$\mathcal{O} \hat{q}^j = \epsilon_e \tilde{A}_s^j (J^{-1})^j (\nabla_\zeta \Delta_\zeta)^2 (J \hat{q})^j \tag{40}$$

and is added to suppress high-frequency oscillations. Here

$$(\nabla_\zeta \Delta_\zeta)^2 q_\ell^j = q_{\ell+2}^j - 4q_{\ell+1}^j + 6q_\ell^j - 4q_{\ell-1}^j + q_{\ell-2}^j \tag{41}$$

If $\alpha = 0$, linear-stability analysis of the dissipation term alone indicates that ϵ_e must be less than $1/8$.

Finally, the difference equations are put into delta form by subtracting $[\tilde{A}_s^j + (1 - \alpha) \Delta \xi (\delta_\zeta \tilde{C}^j - \text{Re}^{-1} \bar{\delta}_\zeta \tilde{M}^j)] \hat{q}^j$ from both sides of the equations. The finished form of the numerical differencing algorithm is then

$$\begin{aligned}
& [\tilde{A}_s^j + (1 - \alpha) \Delta \xi (\delta_\zeta \tilde{C}^j - \text{Re}^{-1} \bar{\delta}_\zeta \tilde{M}^j)] (\hat{q}^{j+1} - \hat{q}^j) \\
& = -(\tilde{A}_s^j - \tilde{A}_s^{j-1}) \hat{q}^j + \alpha (\hat{E}_s^j - \hat{E}_s^{j-1}) - (1 - \alpha) \Delta \xi \{ \delta_\zeta [\zeta_x^{j+1} (E/J)^j + \zeta_z^{j+1} (G/J)^j] \\
& \quad - \text{Re}^{-1} \bar{\delta}_\zeta \tilde{S}^j \} - [(\xi_x/J)^{j+1} E_p^j - (\xi_x/J)^j E_p^{j-1}] + \mathcal{O} \hat{q}^j
\end{aligned} \tag{42}$$

where we have used the fact that $\tilde{M}^j \hat{q}^j = 0$, while on the right-hand side of equation (42), $\tilde{C}^j \hat{q}^j$, defined by equation (33a), was written in terms of the flux vectors. The delta form, in which the left side operates on $\hat{q}^{j+1} - \hat{q}^j = \Delta \hat{q}^j$, is not as efficient as the nondelta version of the difference equation, equation (39). However, the delta form is more convenient in three dimensions, and, as discussed below, higher order spatial accuracy is easily obtained with the delta form algorithm.

Note that the flux vector \hat{G} is not redefined to employ p_s in the subsonic sublayer because experience shows that no inconsistency develops in using the conventional definition of \hat{G} . We remark that q , not E , was used throughout as the dependent variable chiefly because it is awkward to express $G = CA^{-1}E$ in terms of the special sublayer flux vector, E_s . Real gas effects and the viscous terms, especially the turbulent viscosity coefficients, are also more conveniently calculated in terms of q .

For the delta form algorithm, equation (42), in high Reynolds number flow, it is easy to obtain a scheme that is consistent with fourth-order accuracy in the ζ direction. One simply replaces the second-order right-hand side operator δ_ζ of equation (42) with the conventional five-point

LAMINAR
 □ MARCHING CODE
 — TIME-DEPENDENT CODE, REF. 13
 TURBULENT
 ○ MARCHING CODE
 - - - TIME-DEPENDENT CODE, REF. 24

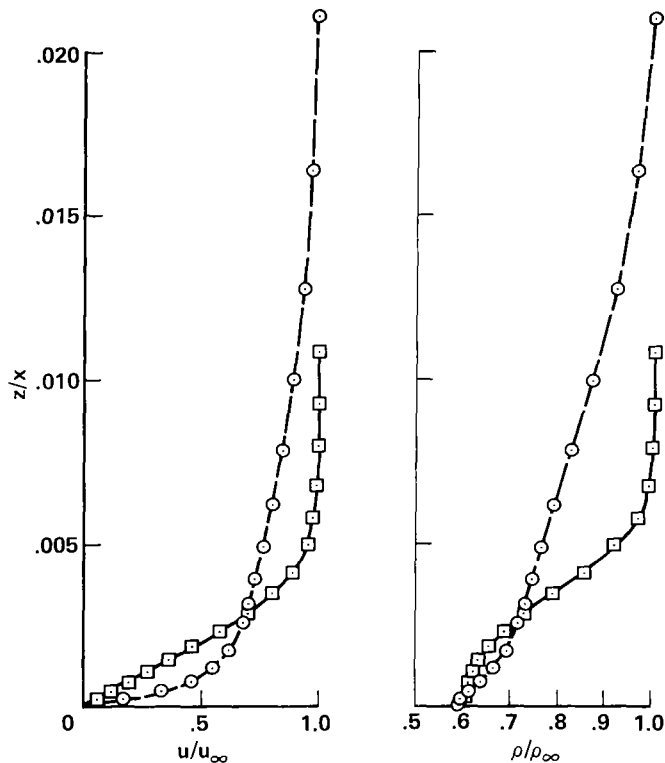


Figure 5.- Flat plate viscous layer profiles; $M_\infty = 2.0$, $Re_x = 0.832 \times 10^6$.

The turbulent marching-code results agree well with the solution obtained by the Steger code (ref. 24) using the same turbulence model.

Nonlifting biconvex airfoil- The capacity of the marching code to handle streamwise variations of geometry was demonstrated by computing the flow over a nonlifting, 10% thick, parabolic arc airfoil. As was done for the flat plate, a turbulent flow was computed at $M_\infty = 2.0$ and $Re_\infty = 1.85 \times 10^6$ based on chord c using the time-dependent code (ref. 24). The computational grid used is shown in figure 3. Flow-field profiles taken at $x/c = 0.10$, $Re_x = 0.185 \times 10^6$ were used as initial data for the marching code, and a marching solution was obtained for $0.10 \leq x/c \leq 1.0$.

The marching and time-dependent surface-pressure distributions, shown in figure 6, demonstrate excellent agreement over the entire airfoil surface. Velocity and density profiles through the viscous layer at $x/c = 0.90$, $Re_x = 1.67 \times 10^6$, are shown in figure 7. Again, good agreement is observed between the marching and time-dependent results. This is not unexpected since, as has been discussed, the normal direction spatial-difference

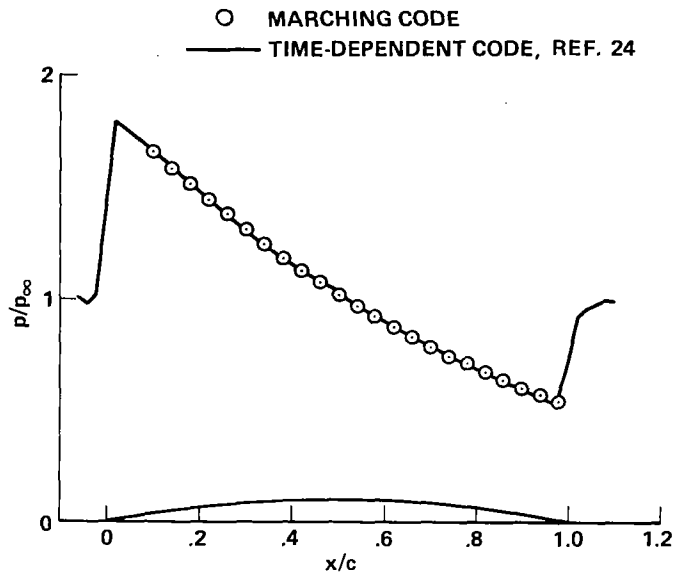


Figure 6.- Parabolic arc airfoil surface-pressure distribution; $M_\infty = 2.0$, $Re_\infty = 1.85 \times 10^6/c$ (turbulent).

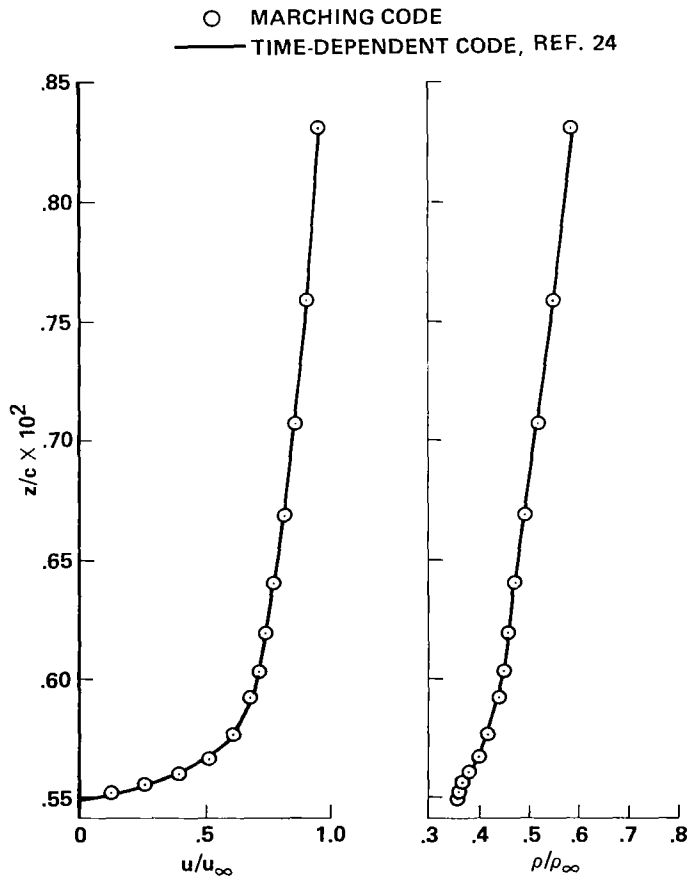


Figure 7.- Parabolic arc airfoil viscous layer profiles; $M_\infty = 2.0$, $Re_x = 1.67 \times 10^6$ (turbulent), $x/c = 0.90$.

operators and the turbulence model of the marching code have the same form as those of the time-dependent code. In addition, the time-dependent results demonstrate that, at each streamwise station, $\partial p/\partial \zeta = 0$ through the subsonic part of the viscous layer, physically justifying the validity of the viscous sublayer approximation made to permit marching.

Departure Solutions and Global Iteration

Although the viscous sublayer method has proved to be accurate and versatile, experience with the sublayer approximation shows that if one continues to refine the marching step size, Δx , the method will ultimately diverge. This is particularly true unless the initial data are very consistent with the sublayer marching equations. The precise cause of the divergence, often called a departure solution, is not settled. An intriguing analysis by Lin and Rubin (ref. 3) suggests that disturbances can amplify when certain integral quantities across the subsonic layer are negative, but it is not clear, at least to us, that their analysis sufficiently models the process of impressing p_s from the stable supersonic region. In any event, we find that the departure-solution behavior can be controlled by using a global-iteration process.

In the global iteration technique one initially specifies an entire p_s distribution. The sublayer marching method (with p_s specified) is then used as part of a relaxation procedure to predict a new flow-field solution and a new p_s distribution. The new p_s distribution is then used to obtain an improved solution, and so on until the new wall shear stress equals that of the previous iteration. Because p_s is specified, any small value of Δx can be used in the marching scheme.

A good initial guess for p_s can be obtained by running the usual sublayer marching procedure with a sufficiently large value of Δx to be stable. Alternatively, a constant value of p_s , corresponding to $\partial p_s/\partial \xi = 0$, can be safely used as an initial guess. Experience with the global iteration technique shows that (1) the solution obtained with the viscous sublayer method for stable values of Δx are usually accurate, and (2) that even if a poor estimate of p_s is initially specified, the global-iteration process is rapidly convergent. In most cases, the pressure distribution is converged after two iterations, and the skin-friction distribution no longer varies after three or four iterations.

The following computations illustrate the additional stability gained from the global-iteration process. The surface-pressure distribution for laminar viscous flow over a 10%-thick biconvex airfoil, at $M_\infty = 2.0$ and $Re_\infty = 1.0 \times 10^6$ based on chord, is shown in figure 8. This solution was computed using the time-dependent code of reference 24. The corresponding velocity profile through the viscous layer at $x/c = 0.8$ is shown in figure 9. A marching solution, obtained using the sublayer approximation for p_s and using $\Delta x = 0.020$, is also shown in figures 8 and 9. The results are in excellent agreement with the time-dependent solution. The marching solution obtained for $\Delta x = 0.010$ is identical to that for $\Delta x = 0.020$, but when

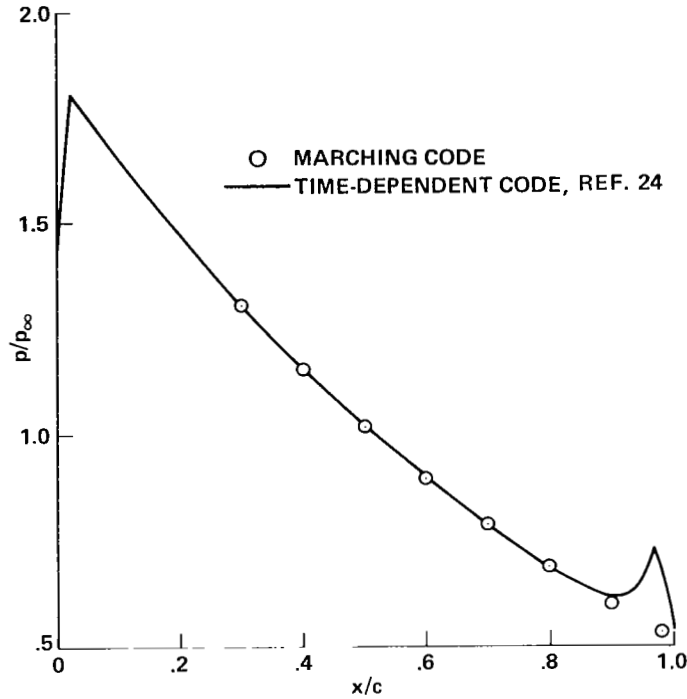


Figure 8.- Surface-pressure distribution on parabolic arc airfoil; $M_\infty = 2.0$, $Re_\infty = 1.0 \times 10^6/c$ (laminar).

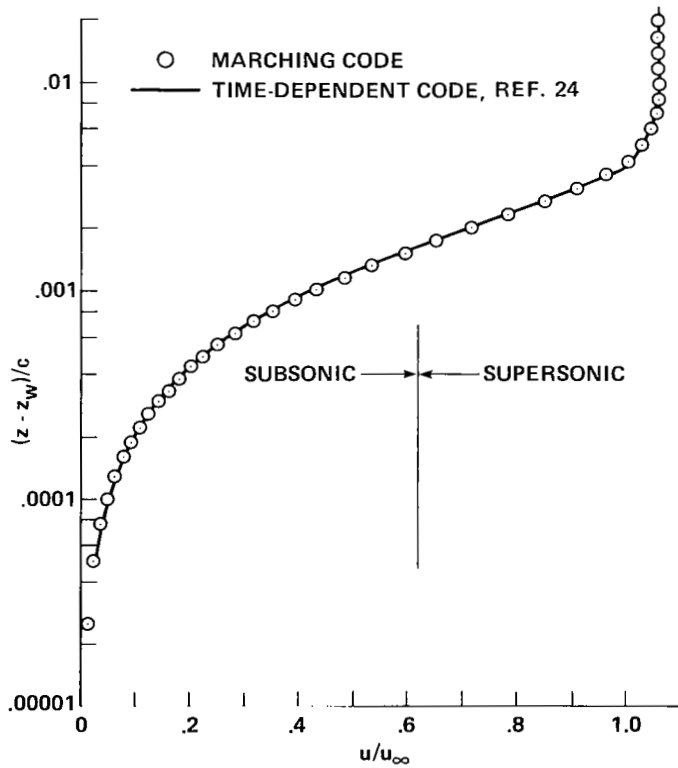


Figure 9.- Viscous layer velocity profile on parabolic arc airfoil, $M_\infty = 2.0$, $Re_x = 0.8 \times 10^6$ (laminar), $x/c = 0.8$.

$\Delta x = 0.005$ was attempted, the solution diverged. However, by using the global iteration procedure, with p_s initially constant, rapidly convergent solutions (identical to the one obtained for $\Delta x = 0.010$) are obtained for the smaller step sizes, $\Delta x = 0.005$ and $\Delta x = 0.00125$. The convergence sequence for the wall shear stress distribution over the first three iterations of the $\Delta x = 0.00125$ case is shown in figure 10.

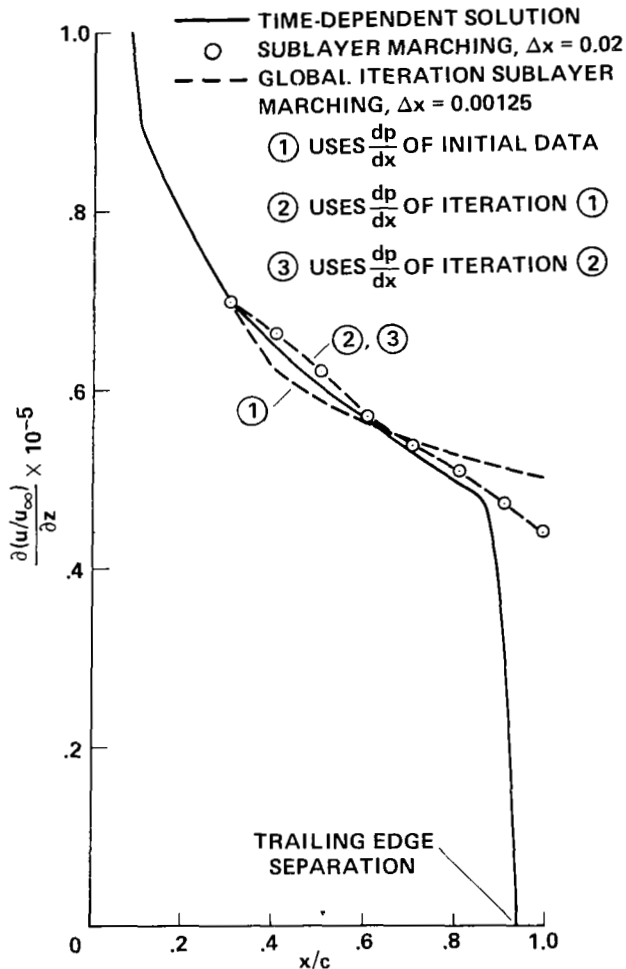


Figure 10.- Velocity gradient distribution on parabolic arc airfoil illustrating global iteration procedure.

three-dimensional boundary-layer flow (see also ref. 3) or for supersonic inviscid flow. One simply has to alter the boundary condition routine and, in the case of inviscid flow, not call the viscous subroutines.

If the time-dependent solution was not available, the global iteration procedure could have been used to show that the stable step size $\Delta x = 0.020$ is sufficiently small to maintain accuracy with the sublayer method. We remark that as the global iteration process is continued in the previous example, the wall-shear stress distribution remains converged to four-place accuracy for the next three global iterations. However, with continued iteration an oscillation will form near the initial profile unless sufficient spatial damping is used. No underrelaxation has been used in the iteration process.

Our preferred solution technique is to use the sublayer approximation and not use the global iteration scheme. However, if in some part of the flow field it becomes necessary to refine Δx to check accuracy, the above global-iteration process can be used economically in that isolated region. By employing the iteration technique only for isolated segments, storage requirements for the p_s distributions can be kept negligible. Moreover, p_s need not be stored at every point in ξ if one is willing to use interpolation.

Boundary-Layer and Inviscid Flow

An added feature of the algorithm developed for the sublayer form of the parabolized Navier-Stokes equations in conservation-law form is that the same computer code can also be used for

The surface boundary condition for inviscid flow is the tangency condition, $W = 0$. Pressure along the body surface can be determined by the normal momentum relation

$$(\zeta_x \zeta_x) \frac{\partial p}{\partial \xi} + (\zeta_x^2 + \zeta_z^2) \frac{\partial p}{\partial \zeta} = -\rho U \left(\zeta_x \frac{\partial u}{\partial \xi} + \zeta_z \frac{\partial w}{\partial \xi} \right) \quad (44)$$

All other body-surface quantities needed for the numerical algorithm can be obtained by simple extrapolations. Because the equations are in strong conservation-law form, shock waves can be captured. However, strong outer bow shocks should be fit in hypersonic flow as numerical oscillations near the shock wave will likely result in negative pressure and density. All of our test calculations have been for supersonic inviscid flow with $M_\infty \leq 2$. As in the case of the parabolized Navier-Stokes equations, inviscid supersonic marching is only valid about bodies with moderate streamwise variation. The calculation should be terminated if a body protuberance (e.g., a canopy) generates a significant embedded subsonic region.

The surface boundary conditions in boundary layer flow are identical to those of the parabolized Navier-Stokes equations. For the direct problem, that is, $p = p_s$ is specified, all of the necessary boundary-layer edge conditions can be obtained from the outer inviscid solution with the exception of W_e . A relation for W_e is obtained by evaluating the continuity equation at the edge, that is

$$\left. \frac{\partial}{\partial \zeta} (\hat{\rho} W) \right|_{\zeta=\zeta_e} = - \frac{\partial}{\partial \xi} \hat{\rho}_e U_e \quad (45)$$

IV. THREE-DIMENSIONAL FLOW

The development of the implicit marching algorithm for steady three-dimensional flow closely parallels the one presented above for two-dimensional flow. The same physical assumptions are made, specifically, neglecting the streamwise derivatives within the viscous terms, and using the sublayer approximation. As we shall demonstrate, the inclusion of the additional spatial coordinate leads to a factored sequence of block-tridiagonal equations, whose block coefficients are now 5×5 matrices.

In this section we merely outline the development of the three-dimensional algorithm, because the extension from two dimensions is straightforward.

Transformed Governing Equations

The three-dimensional steady Navier-Stokes equations, written in nondimensional form, are

$$\frac{\partial \hat{E}}{\partial \xi} + \frac{\partial \hat{F}}{\partial \eta} + \frac{\partial \hat{G}}{\partial \zeta} = \frac{1}{\text{Re}} \left(\frac{\partial \hat{R}}{\partial \xi} + \frac{\partial \hat{T}}{\partial \eta} + \frac{\partial \hat{S}}{\partial \zeta} \right) \quad (46)$$

where

$\xi = \xi(x)$ = streamwise coordinate

$\eta = \eta(x,y,z)$ = spanwise (circumferential) coordinate

$\zeta = \zeta(x,y,z)$ = normal coordinate

and the body is assumed to be mapped onto the $\zeta = 0$ plane (see fig. 11). As before, we neglect the streamwise derivatives within the viscous terms of

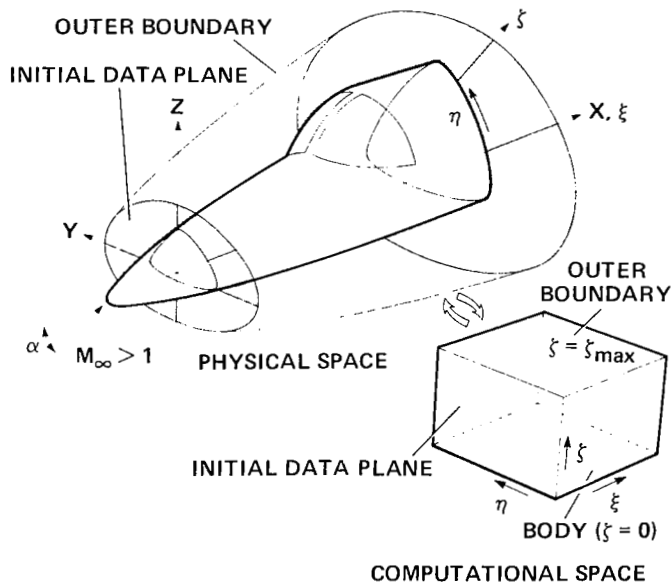


Figure 11.- Transformation of physical space into computational space.

equation (46). This approximation is physically valid for high Reynolds number flows, where streamwise-flow gradients within the subsonic viscous layer are negligible in comparison with those in the normal direction. The same argument permits us also to neglect viscous derivatives along the body in the circumferential direction.

Although it is not necessary to drop the circumferential viscous terms in the development of the parabolized Navier-Stokes approximation, doing so simplifies the computations and is therefore incorporated in the present work. The remaining viscous terms, containing only normal derivatives, constitute the thin-layer model (cf. refs. 19, 24, 25 for further discussion), and can be written as $(1/Re)\partial\hat{S}/\partial\zeta$, where \hat{S} is given by equation (49) below. Introducing the sublayer approximation, the resulting three-dimensional parabolized Navier-Stokes equations can be written as

$$\frac{\partial\hat{E}_s}{\partial\xi} + \frac{\partial\hat{F}}{\partial\eta} + \frac{\partial\hat{G}}{\partial\zeta} = \frac{1}{Re} \frac{\partial\hat{S}}{\partial\zeta} \quad (47)$$

The inviscid flux vectors in equation (47) are

$$\hat{E}_s = \frac{1}{J} \begin{pmatrix} \rho U \\ \rho u U + \xi_x p_s \\ \rho v U \\ \rho w U \\ (e + p_s) U \end{pmatrix}, \quad \hat{F} = \frac{1}{J} \begin{pmatrix} \rho V \\ \rho u V + \eta_x p \\ \rho v V + \eta_y p \\ \rho w V + \eta_z p \\ (e + p) V \end{pmatrix}, \quad \hat{G} = \frac{1}{J} \begin{pmatrix} \rho W \\ \rho u W + \zeta_x p \\ \rho v W + \zeta_y p \\ \rho w W + \zeta_z p \\ (e + p) W \end{pmatrix}, \quad \hat{q} = \frac{1}{J} \begin{pmatrix} \rho \\ \rho u \\ \rho v \\ \rho w \\ e \end{pmatrix} \quad (48)$$

The thin-layer model viscous term is

$$\hat{S} = \frac{1}{J} \begin{pmatrix} 0 \\ \mu(\zeta_x^2 + \zeta_y^2 + \zeta_z^2)u_\zeta + (\mu/3)(\zeta_x u_\zeta + \zeta_y v_\zeta + \zeta_z w_\zeta)\zeta_x \\ \mu(\zeta_x^2 + \zeta_y^2 + \zeta_z^2)v_\zeta + (\mu/3)(\zeta_x u_\zeta + \zeta_y v_\zeta + \zeta_z w_\zeta)\zeta_y \\ \mu(\zeta_x^2 + \zeta_y^2 + \zeta_z^2)w_\zeta + (\mu/3)(\zeta_x u_\zeta + \zeta_y v_\zeta + \zeta_z w_\zeta)\zeta_z \\ \{(\zeta_x^2 + \zeta_y^2 + \zeta_z^2)[(\mu/2)(u^2 + v^2 + w^2)_\zeta + \kappa \text{Pr}^{-1}(\gamma - 1)^{-1}(a^2)_\zeta] \\ + (\mu/3)(\zeta_x u + \zeta_y v + \zeta_z w)(\zeta_x u_\zeta + \zeta_y v_\zeta + \zeta_z w_\zeta)\} \end{pmatrix} \quad (49)$$

and

$$p_s = (\gamma - 1)[e - 0.5\rho(u^2 + v^2 + w^2)] \quad , \quad u > a(1 + \epsilon_s)$$

or

$$\frac{\partial p}{\partial \zeta} = 0 \quad , \quad u < a(1 + \epsilon_s)$$

The metric terms are obtained from chain-rule expansion of x_ξ , y_η , etc., and are solved for ξ_x , η_y , etc., to give

$$\left. \begin{aligned} \xi_x &= \frac{1}{x_\xi} \\ \eta_x &= J(z_\xi y_\zeta - y_\xi z_\zeta) & \zeta_x &= J(y_\xi z_\eta - z_\xi y_\eta) \\ \eta_y &= J(x_\xi z_\zeta) & \zeta_y &= -J(x_\xi z_\eta) \\ \eta_z &= -J(x_\xi y_\zeta) & \zeta_z &= J(x_\xi y_\eta) \end{aligned} \right\} \quad (50)$$

and

$$\frac{1}{J} = x_\xi (y_\eta z_\zeta - y_\zeta z_\eta) \quad (51)$$

Here the contravariant velocities U , V , and W assume the form

$$\left. \begin{aligned} U &= \xi_x u \\ V &= \eta_x u + \eta_y v + \eta_z w \\ W &= \zeta_x u + \zeta_y v + \zeta_z w \end{aligned} \right\} \quad (52)$$

The Jacobian matrices \hat{A} , \hat{B} , and \hat{C} , needed in the linearization of \hat{E} , \hat{F} , and \hat{G} , can be written as

$$\hat{A}, \hat{B}, \text{ or } \hat{C} = \begin{bmatrix} 0 & K_1 & K_2 & K_3 & 0 \\ K_1 \phi^2 - u\theta & \theta - K_1(\gamma - 2)u & K_2 u - (\gamma - 1)K_1 v & K_3 u - (\gamma - 1)K_1 w & K_1(\gamma - 1) \\ K_2 \phi^2 - v\theta & K_1 v - K_2(\gamma - 1)u & \theta - K_2(\gamma - 2)v & K_3 v - (\gamma - 1)K_2 w & K_2(\gamma - 1) \\ K_3 \phi^2 - w\theta & K_1 w - K_3(\gamma - 1)u & K_2 w - K_3(\gamma - 1)v & \theta - K_3(\gamma - 2)w & K_3(\gamma - 1) \\ \theta[2\phi^2 - \gamma(e/\rho)] & \{K_1[\gamma(e/\rho) - \phi^2] \\ & - (\gamma - 1)u\theta\} & \{K_2[\gamma(e/\rho) - \phi^2] \\ & - (\gamma - 1)v\theta\} & \{K_3[\gamma(e/\rho) - \phi^2] \\ & - (\gamma - 1)w\theta\} & \gamma\theta \end{bmatrix} \quad (53)$$

where $\phi^2 = 0.5(\gamma - 1)(u^2 + v^2 + w^2)$, $\theta = K_1 u + K_2 v + K_3 w$ and, for example, to obtain \hat{C} , $K_1 = \zeta_x$, $K_2 = \zeta_y$, $K_3 = \zeta_z$.

The viscous vector \hat{S} is linearized by Taylor series as in reference 24, producing the coefficient matrix operator

$$\hat{M} = \frac{1}{J} \begin{bmatrix} 0 & 0 & 0 & 0 & 0 \\ m_{21} & \alpha_1 \delta_\zeta(1/\hat{\rho}) & \alpha_2 \delta_\zeta(1/\hat{\rho}) & \alpha_3 \delta_\zeta(1/\hat{\rho}) & 0 \\ m_{31} & \alpha_2 \delta_\zeta(1/\hat{\rho}) & \alpha_4 \delta_\zeta(1/\hat{\rho}) & \alpha_5 \delta_\zeta(1/\hat{\rho}) & 0 \\ m_{41} & \alpha_3 \delta_\zeta(1/\hat{\rho}) & \alpha_5 \delta_\zeta(1/\hat{\rho}) & \alpha_6 \delta_\zeta(1/\hat{\rho}) & 0 \\ m_{51} & m_{52} & m_{53} & m_{54} & \alpha_0 \delta_\zeta(1/\hat{\rho}) \end{bmatrix} \quad (54)$$

with

$$\begin{aligned} m_{21} &= \alpha_1 \delta_\zeta(-u/\hat{\rho}) + \alpha_2 \delta_\zeta(-v/\hat{\rho}) + \alpha_3 \delta_\zeta(-w/\hat{\rho}) \\ m_{31} &= \alpha_2 \delta_\zeta(-u/\hat{\rho}) + \alpha_4 \delta_\zeta(-v/\hat{\rho}) + \alpha_5 \delta_\zeta(-w/\hat{\rho}) \\ m_{41} &= \alpha_3 \delta_\zeta(-u/\hat{\rho}) + \alpha_5 \delta_\zeta(-v/\hat{\rho}) + \alpha_6 \delta_\zeta(-w/\hat{\rho}) \\ m_{51} &= \alpha_1 \delta_\zeta(-u^2/\hat{\rho}) + \alpha_2 \delta_\zeta(-2uv/\hat{\rho}) + \alpha_3 \delta_\zeta(-2uw/\hat{\rho}) \\ &\quad + \alpha_4 \delta_\zeta(-v^2/\hat{\rho}) + \alpha_6 \delta_\zeta(-w^2/\hat{\rho}) + \alpha_5 \delta_\zeta(-2vw/\hat{\rho}) \\ &\quad + \alpha_0 \delta_\zeta(-\hat{e}/\hat{\rho}^2) + \alpha_0 \delta_\zeta[(u^2 + v^2 + w^2)/\hat{\rho}] \end{aligned}$$

$$\begin{aligned}
m_{52} &= -m_{21} - \alpha_0 \delta_\zeta (u/\hat{\rho}) , & m_{53} &= -m_{31} - \alpha_0 \delta_\zeta (v/\hat{\rho}) \\
m_{54} &= -m_{41} - \alpha_0 \delta_\zeta (w/\hat{\rho}) \\
\alpha_0 &= \gamma \kappa \text{Pr}^{-1} (\zeta_x^2 + \zeta_y^2 + \zeta_z^2) , & \alpha_1 &= \mu [(4/3)\zeta_x^2 + \zeta_y^2 + \zeta_z^2] \\
\alpha_2 &= (\mu/3)\zeta_x \zeta_y , & \alpha_3 &= (\mu/3)\zeta_x \zeta_z \\
\alpha_4 &= \mu [\zeta_x^2 + (4/3)\zeta_y^2 + \zeta_z^2] , & \alpha_5 &= (\mu/3)\zeta_y \zeta_z \\
\alpha_6 &= \mu [\zeta_x^2 + \zeta_y^2 + (4/3)\zeta_z^2]
\end{aligned}$$

Finally, the sublayer Jacobian matrix $A_u \equiv [\partial E_s / \partial q]$ is given by

$$A_u = \begin{bmatrix} 0 & 1 & 0 & 0 & 0 \\ -u^2 & 2u & 0 & 0 & 0 \\ -uv & v & u & 0 & 0 \\ -uw & w & 0 & u & 0 \\ -u(e + p_s)/\rho & (e + p_s)/\rho & 0 & 0 & u \end{bmatrix} \quad (55)$$

and again all the eigenvalues of A_u are equal to u .

Numerical Algorithm and Solution Procedure

The implicit marching algorithm for the solution of equation (47) is derived in the same manner as its two-dimensional counterpart, with the \hat{F} flux vector linearized in the same manner as \hat{G} . The resulting algorithm, written in delta form, is

$$\begin{aligned}
& [\tilde{A}_s^j + (1 - \alpha)\Delta\xi(\delta_\eta \tilde{B}^j + \delta_\zeta \tilde{C}^j - \text{Re}^{-1} \delta_\zeta \tilde{M}^j)] (\hat{q}^{j+1} - \hat{q}^j) \\
& = -(\tilde{A}_s^j - \tilde{A}_s^{j-1}) \hat{q}^j + \alpha (\hat{E}_s^j - \hat{E}_s^{j-1}) \\
& \quad - (1 - \alpha)\Delta\xi \left\{ \delta_\eta [\eta_x^{j+1} (E/J)^j + \eta_y^{j+1} (F/J)^j + \eta_z^{j+1} (G/J)^j] \right. \\
& \quad \left. + \delta_\zeta [\zeta_x^{j+1} (E/J)^j + \zeta_y^{j+1} (F/J)^j + \zeta_z^{j+1} (G/J)^j] - \text{Re}^{-1} \delta_\zeta \tilde{S}^j \right\} \\
& \quad - [(\xi_x/J)^{j+1} E_p^j - (\xi_x/J)^j E_p^{j-1}] + \mathcal{D} \hat{q}^j \quad (56)
\end{aligned}$$

where δ_η is central differenced like δ_ζ , equation (28), and the smoothing term \mathcal{D} is defined by

$$\mathcal{D} = \epsilon_e \tilde{A}_{S_{k,\ell}}^j \left(\frac{1}{J} \right)^j [(\nabla_\eta \Delta_\eta)^2 (J\hat{q})^j + (\nabla_\zeta \Delta_\zeta)^2 (J\hat{q})^j]$$

Here ϵ_e must be less than 1/16 for stability.

An approximately-factored form of equation (56), which retains the same order of accuracy in ξ , can be obtained if we note that

$$\begin{aligned} \left[\tilde{A}_S^j + (1 - \alpha) \Delta \xi (\delta_\eta \tilde{B}^j) \right] (\tilde{A}_S^j)^{-1} \left[\tilde{A}_S^j + (1 - \alpha) \Delta \xi (\delta_\zeta \tilde{C}^j - \text{Re}^{-1} \bar{\delta}_\zeta \tilde{M}^j) \right] \Delta \hat{q}^j \\ = \text{LHS}(56) + O(\Delta \xi)^3 \end{aligned} \quad (57)$$

(Note: A_S^{-1} can degrade the factorization error if u is sufficiently small.) On replacing the left side of equation (56), LHS(56), with the left side of equation (57), one obtains the factored algorithm. The algorithm is solved by the sequence of implicit inversions

$$\left[\tilde{A}_S^j + (1 - \alpha) \Delta \xi (\delta_\eta \tilde{B}^j) \right] \Delta \hat{q}_* = \text{RHS}(56) \quad (58a)$$

$$\left[\tilde{A}^j + (1 - \alpha) \Delta \xi (\delta_\zeta \tilde{C}^j - \text{Re}^{-1} \bar{\delta}_\zeta \tilde{M}^j) \right] \Delta \hat{q}^j = A_S^j \Delta \hat{q}_* \quad (58b)$$

Equation (58) differs from its two-dimensional analogy primarily in the inclusion of the implicit circumferential inversion factor.

A typical computational grid is shown in the physical crossflow plane [$x = x_0(\xi_0)$] in figure 12. The grid extends radially between the body

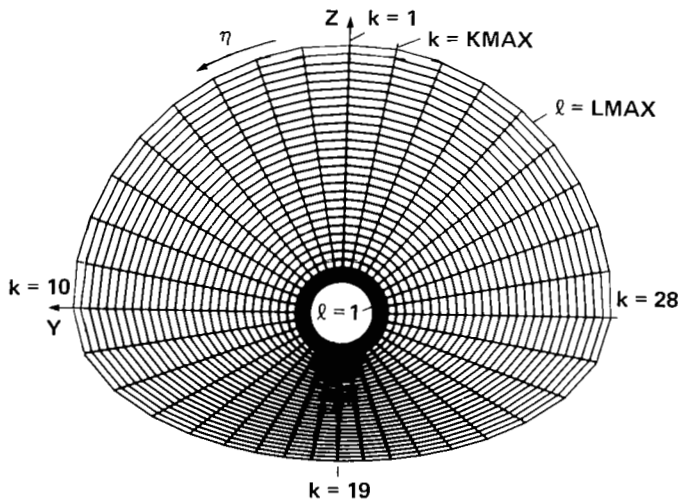


Figure 12.- Cross-section of typical computational grid, $x = x_0(\xi_0)$.

surface and an outer boundary located in the undisturbed free stream, and is chosen to completely circumscribe the body, $1 \leq k \leq KMAX$, to permit a treatment of nonbilaterally-symmetric flows. Such flows include the case of combined angles of attack and yaw, and the important case of a non-symmetric leeward side wake exhibited by axisymmetric bodies at large incidence. Symmetric flows can be treated with half the computational effort by employing a grid that runs from the windward to leeward plane of symmetry and by applying the usual symmetry conditions at the edges.

To advance the solution of equation (58), we first form the right-hand side terms of equation (58a) and perform the circumferential implicit inversion. The use of a central difference approximation for the η derivatives, together with the periodic continuation condition, leads to a periodic block-tridiagonal system of equations. This system is inverted, using the solver described in reference 26, to obtain the intermediate variables. Once these quantities are known, the right-hand side terms of equation (58b), $A_S^j \Delta \hat{q}_*$, are evaluated, and the equation is inverted in the normal direction, using the same procedure previously described for equation (42), to obtain $\Delta \hat{q}_{k,\ell}^j$, and thus $q_{k,\ell}^{j+1}$.

Three-Dimensional Results

The accuracy of the factored marching algorithm applied to three-dimensional flow was evaluated by computing the flow field about a hemisphere-cylinder body at 0° and at 5° angle of attack. The test-case conditions were again chosen to duplicate steady flow-field results obtained from time-dependent Navier-Stokes computations and, for the body at incidence, to match those of the wind-tunnel experiment described in reference 27.

Axisymmetric flow- Although the flow field surrounding the hemisphere cylinder at zero incidence is axisymmetric, the Cartesian velocity components used in the computation vary sinusoidally in the circumferential direction around the body. Thus, this case provides a nontrivial test of the factorization procedure. The azimuthal-invariant time-dependent code, described in reference 28, was used to compute the turbulent flow around the body, at $M_\infty = 2.0$ and $Re_\infty = 8.80 \times 10^4$ based on nose radius R_N , using the grid shown in longitudinal section in figure 13. The flow field exhibits an embedded subsonic region in the shock layer at the nose, which expands around the nose and becomes supersonic in the vicinity of the sphere-cylinder junction. Flow profiles taken at $x/R_N = 3.45$, downstream of the subsonic region, were used as initial data for the marching code, and a marching solution was obtained for $3.45 \leq x/R_N \leq 21.0$

The marching and time-dependent surface-pressure distributions are shown in figure 14 and are in good agreement over the entire body. The small axial oscillation in the marching results is attributed to a small inconsistency between the initial data and the marching technique. The amplitude of the oscillation is never more than 1% of the pressure and is seen to damp toward the rear of the body. Velocity and density profiles within the viscous layer,

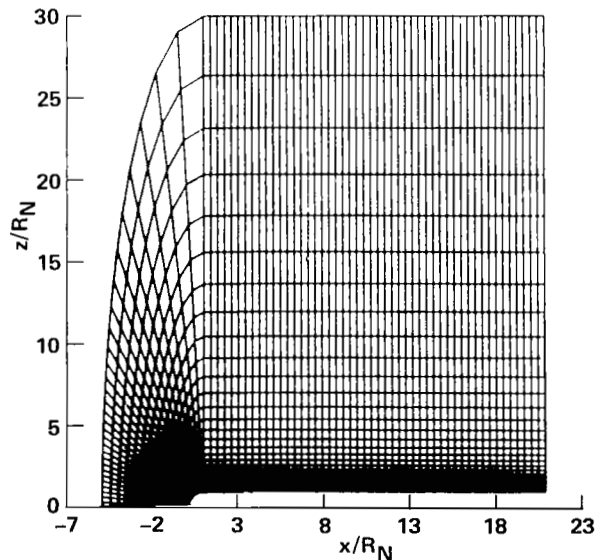


Figure 13.- Axisymmetric hemisphere cylinder computational mesh.

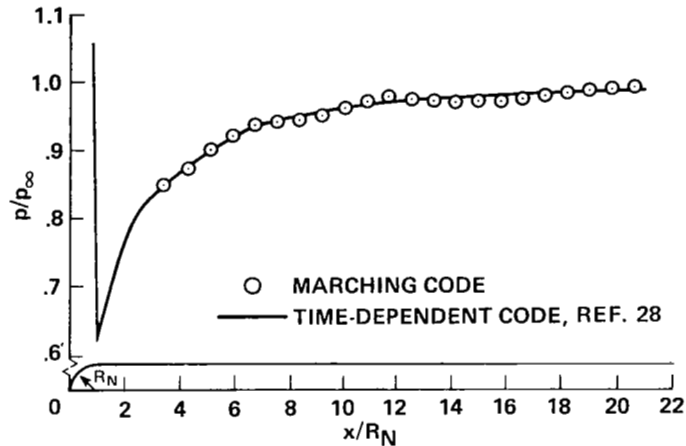


Figure 14.- Axisymmetric hemisphere cylinder surface-pressure distribution;
 $M_\infty = 2.0$, $Re_\infty = 8.80 \times 10^4 / R_N$ (turbulent).

taken from the marching and time-dependent solutions at $x/R_N = 20.6$, are shown in figure 15. The marching results show good agreement with those of the time-dependent code.

Hemisphere cylinder at incidence- The flow field surrounding a hemisphere cylinder at incidence in a low-Mach-number supersonic stream has recently been investigated experimentally by Hsieh (ref. 27), and computationally by Pulliam and Steger (ref. 25), who used a three-dimensional, time-dependent, thin-layer Navier-Stokes code. Their computational grid was selected to resolve the details of the flow in the region of the nose, and in this region the computed results are in good agreement with the experimental measurements. However, the limitation of computer storage required that the grid be progressively stretched axially along the cylinder. Consequently, the streamwise details of the downstream flow were only marginally resolved. The use of the marching code, with initial data taken from the time-dependent solution in a region of good resolution, can circumvent the storage limitations. Using a grid similar to that shown in figure 13, a steady turbulent flow solution was obtained using the time-dependent code (ref. 25) at $M_\infty = 1.40$, $Re_\infty = 2.0 \times 10^5$ based on R_N , and $\alpha = 5^\circ$. Data taken at $x/R_N = 3.07$ were prescribed as initial data and a marching solution was obtained from $3.07 \leq x/R_N \leq 40.0$. A comparison of the surface-pressure distributions along the windward and leeward planes of symmetry is shown in figure 16, together with the experiments of Hsieh (ref. 27). Although the marching solution was obtained for $x/R_N \leq 40.0$, and could be continued downstream, only the data for the region where the marching results, the time-dependent results, and the experimental measurements overlap, $3.07 \leq x/R_N \leq 16.0$, are presented in figure 16. The marching results are in good agreement with the time-dependent results in the region common to both computations, $x/R_N \leq 14.0$, and both are in good agreement with the measured surface pressures. However, the marching-code results give better agreement with the measured values for $9.0 \leq x/R_N \leq 14.0$, where the time-dependent solution lacks resolution.

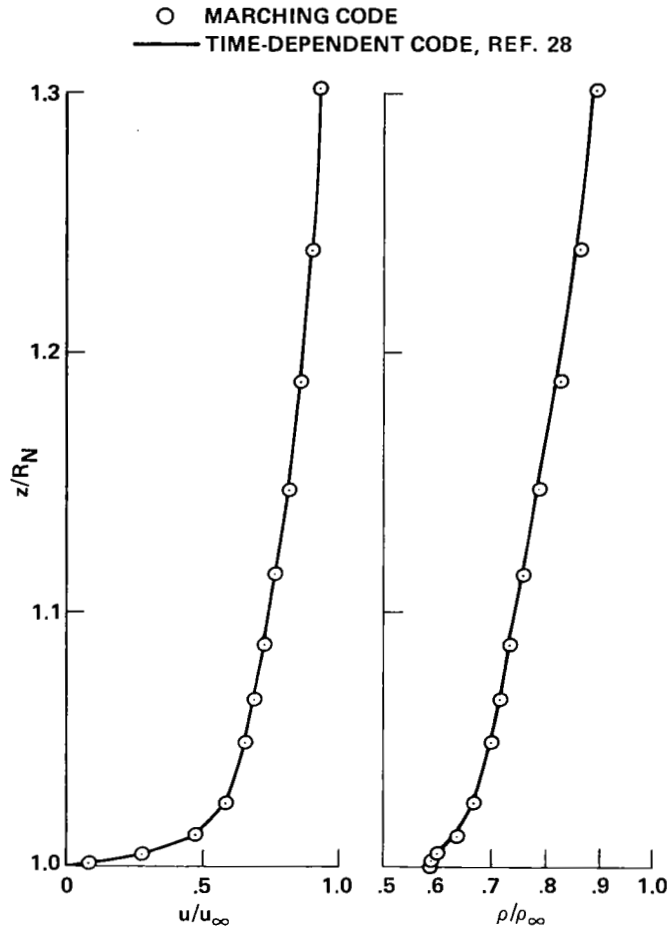


Figure 15.- Axisymmetric hemisphere cylinder viscous layer profiles; $M_\infty = 2.0$, $Re_x = 1.81 \times 10^5$ (turbulent), $x/R_N = 20.6$.

Streamwise velocity profiles through the viscous layer on the windward and leeward rays, taken from the computational results at $x/R_N = 6.98$, are shown in figure 17. At this axial location, the stretched grid of the time-dependent solution still maintains adequate streamwise resolution. The velocity gradient is much more sensitive than is surface pressure. Thus, the good agreement between the time-dependent and the marching solutions attests to the accuracy of the factored marching algorithm. Also, the time-dependent results exhibit constant pressure across the subsonic viscous layer, thus justifying the assumptions made in the viscous sublayer approximation.

Conical Flow Fields

Motivation- The initial data for the marching method must, in general, be supplied from an auxiliary, time-dependent computation. However, when considering flow over conical or pointed bodies, the marching technique can be used to generate its own initial data. For example, inviscid conical solutions can

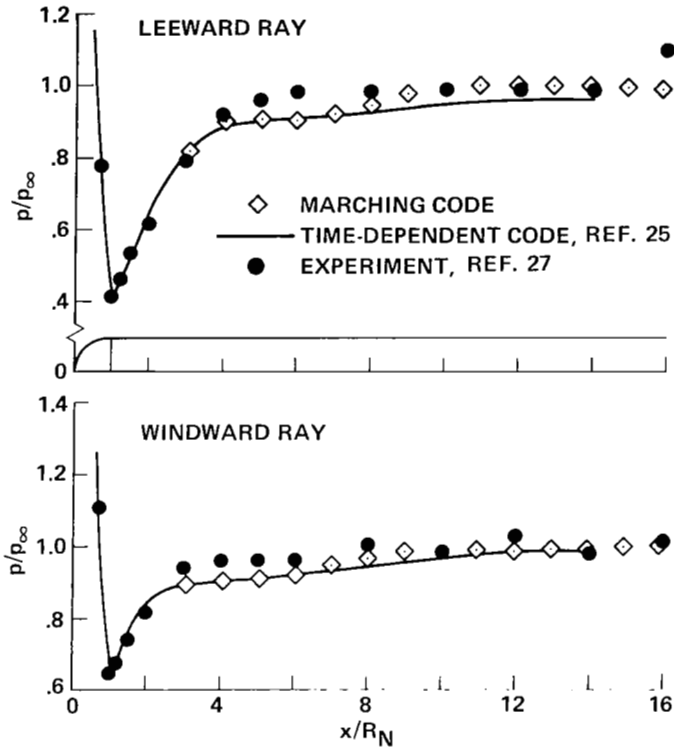


Figure 16.- Windward and leeward symmetry plane surface-pressure distributions on hemisphere cylinder at incidence; $M_\infty = 1.40$, $Re_\infty = 2.0 \times 10^5 / R_N$ (turbulent), $\alpha = 5^\circ$.

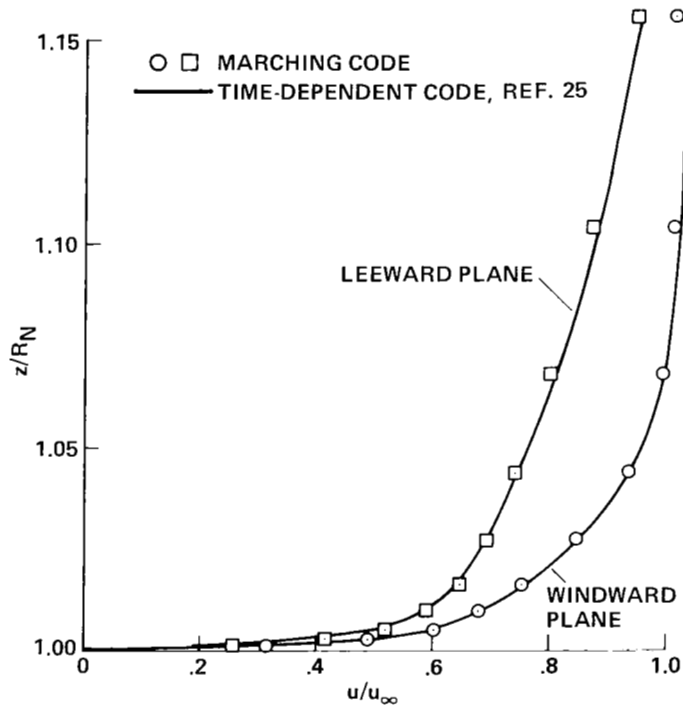


Figure 17.- Viscous layer velocity profiles on hemisphere cylinder at incidence; $M_\infty = 1.40$, $Re_x = 1.40 \times 10^6$ (turbulent), $x/R_N = 6.98$, $\alpha = 5^\circ$.

be obtained by using the marching method as a distance-asymptotic technique. The computational grid is chosen to be conical, with grid points at successive axial stations located along rays emanating from the cone apex (see fig. 18). The flow variables are initially set to free-stream values and the equations are marched downstream from $x = x_0$ to $x = x_0 + \Delta x$. After each step, the solution is scaled to place it back at the initial station, $x = x_0$. When no change in the flow variables occurs with further marching, the flow variables are constant along rays, and a conical flow field has been obtained.

If conditions within the viscous layer are also assumed to be conical (see ref. 29 for discussion and ref. 30 for experimental confirmation for high Reynolds number flows), the marching step-back procedure can be used to generate conical viscous flows. Here, the assumption of conical flow permits setting $\partial p_s / \partial \xi = 0$ within the subsonic viscous layer. In this case, the marching step-back method is numerically equivalent to that of McRae (ref. 29), in which the Navier-Stokes equations are written in conical coordinates, derivatives along rays are dropped, and the resulting equations are advanced in time to obtain a steady solution.

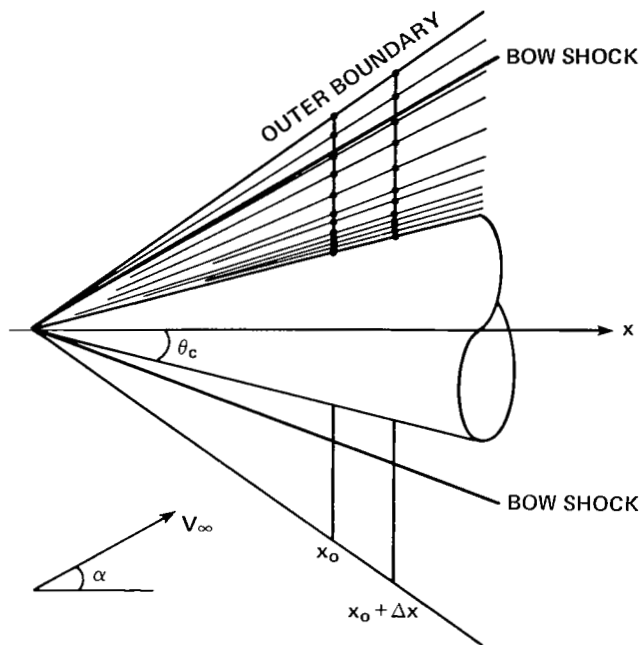


Figure 18.- Conical flow grid.

Conical results- A series of computations was performed to obtain laminar flows over a 9.09° half-angle cone at $M_\infty = 2.0$, $Re_x = 1.85 \times 10^5$ based on axial distance from the nose, and for angles of attack ranging from 0° to 15° . The computational grid completely encircled the body and the resulting flows were found to be symmetric about the windward plane.

The circumferential surface-pressure distribution found for $\alpha = 10^\circ$ is shown in figure 19, and is in good agreement with the corresponding results obtained by McRae (private communication, AFFDL, Ames Research Center, Moffett Field, Calif., 1978). Pressure contours in the crossflow plane, $x = x_0$, of the marching solution are shown in figure 20, and demonstrate the symmetry of the flow.

At 10° angle of attack, a small reversed crossflow-separation region occurs near the leeward plane of symmetry. This can be seen in figure 21, which presents the projections of the flow velocity vectors onto the crossflow plane for points near the body surface. The location of the circumferential

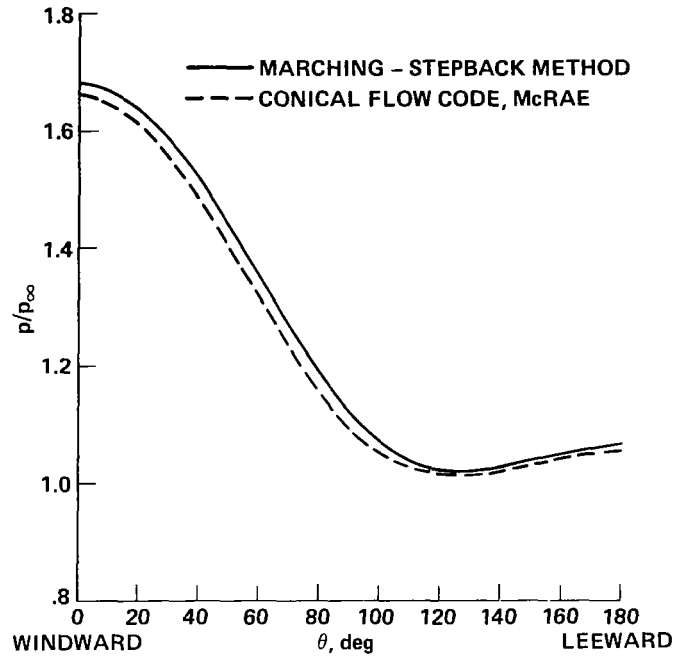


Figure 19.- Circumferential surface-pressure distribution on 9.09° half-angle cone; $M_\infty = 2.0$, $Re_x = 1.85 \times 10^5$ (laminar), $\alpha = 10^\circ$.

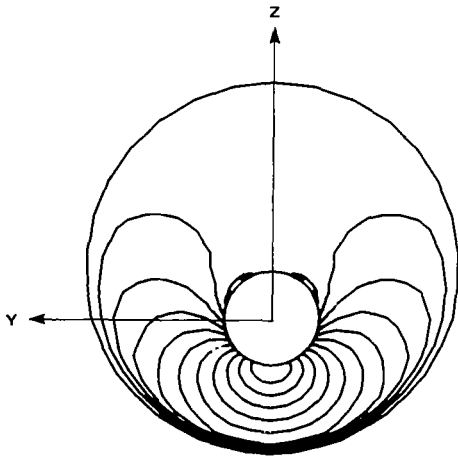


Figure 20.- Crossflow plane pressure contours; $\theta_c = 9.09^\circ$, $M_\infty = 2.0$, $Re_x = 1.85 \times 10^5$ (laminar), $\alpha = 10^\circ$.

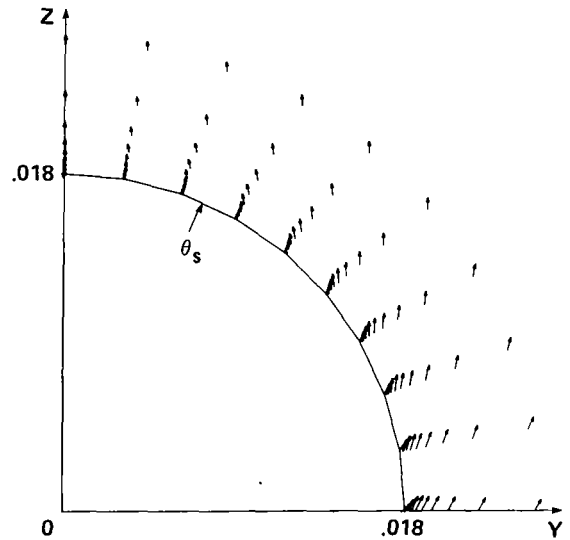


Figure 21.- Crossflow plane velocity vectors; $\theta_c = 9.09^\circ$, $M_\infty = 2.0$, $Re_x = 1.85 \times 10^5$ (laminar), $\alpha = 10^\circ$.

separation point θ_s , obtained by interpolation, is also indicated in figure 21.

The circumferential surface-pressure distribution and crossflow velocity vectors for $\alpha = 15^\circ$ are shown in figures 22 and 23, respectively. At this angle of attack, relative incidence $\alpha/\theta_c = 1.65$, the crossflow separation region is more pronounced radially. Also the crossflow separation point is located closer to the windward symmetry plane.

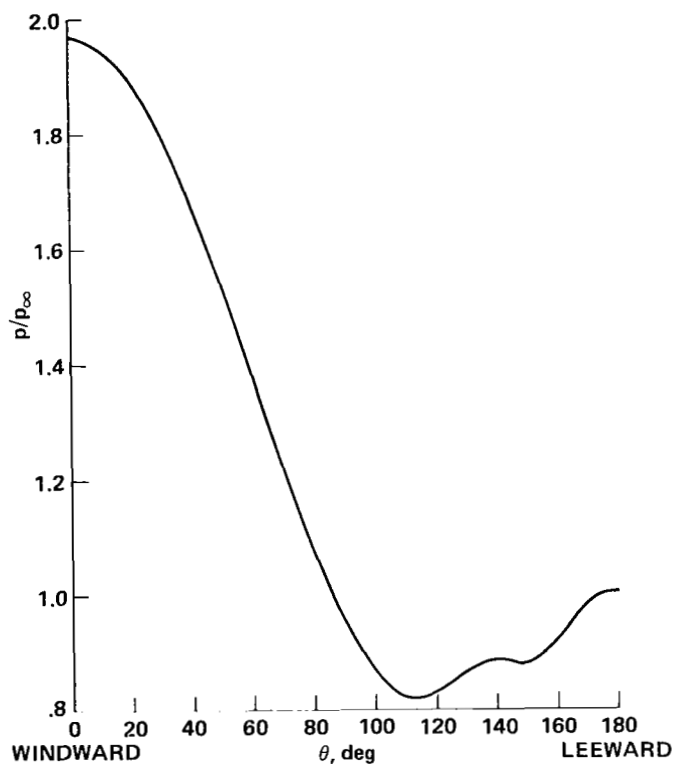


Figure 22.- Circumferential surface-pressure distribution; $\theta_c = 9.09^\circ$, $M_\infty = 2.0$, $Re_x = 1.85 \times 10^5$ (laminar), $\alpha = 15^\circ$.

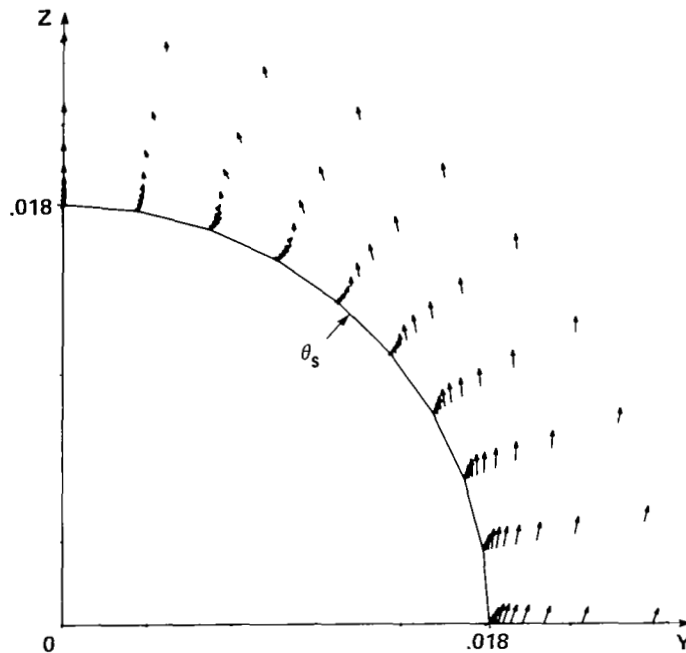


Figure 23.- Crossflow plane velocity vectors; $\theta_c = 9.09^\circ$, $M_\infty = 2.0$,
 $Re_x = 1.85 \times 10^5$ (laminar), $\alpha = 15^\circ$.

V. CONCLUDING REMARKS

A noniterative, implicit, finite-difference marching algorithm has been developed for steady supersonic viscous flow. The parabolized Navier-Stokes equations, in strong conservation-law form, have been transformed into general coordinates so that arbitrary body shapes can be mapped onto constant planes in the uniform computational space. The approximately factored finite-difference algorithm is noniterative, second-order accurate in the marching direction, and second- or fourth-order accurate in the crossflow plane. Use of the subsonic layer approximation with a global iteration technique for "surface" pressure allows the grid spacing to be refined in a uniform manner.

Ames Research Center
 National Aeronautics and Space Administration
 Moffett Field, Calif. 94035, May 8, 1980

REFERENCES

1. Cheng, H. K.; Chen, S. Y.; Mobley, R.; and Huber, C.: The Viscous Hypersonic Slender-Body Problem: A Numerical Approach Based on a System of Composite Equations. RM 6193-PR, The Rand Corp., 1970.
2. Rubin, S. G.; and Lin, T. C.: Numerical Methods for Two- and Three-Dimensional Viscous Flow Problems: Application to Hypersonic Leading Edge Equations. PIBAL Rep. 71-8 (AFOSR-TR-71-0778), 1971.
3. Lin, T. C.; and Rubin, S. G.: Viscous Flow Over a Cone at Moderate Incidence: I. Hypersonic Tip Region. Computers and Fluids, vol. 1, 1973, pp. 37-57.
4. Nardo, C. T.; and Cresci, R. J.: An Alternating Directional Implicit Scheme for Three-Dimensional Hypersonic Flows. J. Comput. Phys., vol. 8, 1971, pp. 268-284.
5. Lubard, S. C.; and Helliwell, W. S.: Calculation of the Flow on a Cone at High Angle of Attack. AIAA J., vol. 12, no. 7, 1974, pp. 965-974.
6. Vignerot, Y. C.; Rakich, J. V.; and Tannehill, J. C.: Calculation of Supersonic Viscous Flow Over Delta Wings with Sharp Subsonic Leading Edges. AIAA Paper 78-1137, 1978.
7. Patankar, S. V.; and Spalding, D. B.: A Calculation Procedure for Heat, Mass and Momentum Transfer in Three-Dimensional Parabolic Flows. Int. J. Heat Mass Trans., vol. 15, 1972, pp. 1787-1806.
8. McDonald, H.; and Briley, W. R.: Three-Dimensional Supersonic Flow of a Viscous or Inviscid Gas. J. Comput. Phys., vol. 19, 1975, pp. 150-178.
9. Briley, W. R.: Numerical Method for Predicting Three-Dimensional Steady Viscous Flow in Ducts. J. Comput. Phys., vol. 14, 1974, pp. 8-28.
10. Kreskovsky, J. P.; and Shamroth, S. J.: An Implicit Marching Method for the Two-Dimensional Reduced Navier-Stokes Equations at Arbitrary Mach Number. Computer Methods in Applied Mechanics and Engineering, vol. 13, 1978, pp. 307-334.
11. Roberts, D. W.; and Forester, C. K.: A Parabolic Computational Procedure for Three-Dimensional Flows in Ducts with Arbitrary Cross Section. AIAA Paper 78-143, 1978.
12. Birch, S. F.; Paynter, G. C.; Spalding, D. B.; and Tatchell, D. G.: Numerical Modeling of Three-Dimensional Flows in Turbofan Engine Exhaust Nozzles. J. Aircraft, vol. 15, no. 8, 1978, pp. 489-496.

13. Beam, R.; and Warming, R. F.: An Implicit Factored Scheme for the Compressible Navier-Stokes Equations. AIAA J., vol. 16, no. 4, 1978, pp. 393-402.
14. Warming, R. F.; and Beam, R.: On the Construction and Application of Implicit Factored Schemes for Conservation Laws. SIAM-AMS Proc., vol. 11, Proc. Symposium on Computational Fluid Mechanics, New York, 1977, pp. 85-129.
15. Peyret, R.; and Viviand, H.: Computation of Viscous Compressible Flows Based on the Navier-Stokes Equations. AGARD-AG-212, 1975.
16. Viviand, H.: Conservative Forms of Gas Dynamic Equations. La Recherche Aeronautique, no. 1, 1974, pp. 65-68.
17. Rudman, S.; and Rubin, S. G.: Hypersonic Viscous Flow over Slender Bodies with Sharp Leading Edges. AIAA J., vol. 6, no. 10, 1968, pp. 1883-1890.
18. Davis, R. T.: Numerical Solution of the Hypersonic Viscous Shock-Layer Equations. AIAA J., vol. 8, no. 5, 1970, pp. 843-851.
19. Baldwin, B. S.; and Lomax, H.: Thin Layer Approximation and Algebraic Model for Separated Turbulent Flows. AIAA Paper 78-257, 1978.
20. Steger, J. L.: Coefficient Matrices for Implicit Finite Difference Solution of the Inviscid Fluid Conservation Law Equations. Computer Methods in Applied Mechanics and Engineering, vol. 13, 1978, pp. 175-188.
21. Garabedian, P. R.: Partial Differential Equations. John Wiley and Sons, 1964.
22. Hall, G.; and Watt, J. M., eds.: Modern Numerical Methods for Ordinary Differential Equations. Clarendon Press, Oxford, 1976.
23. Gear, C. W.: Numerical Initial Value Problems in Ordinary Differential Equations. Prentice-Hall Inc., 1971.
24. Steger, J. L.: Implicit Finite-Difference Simulation of Flow About Arbitrary Two-Dimensional Geometries. AIAA J., vol. 16, no. 7, 1978, pp. 679-686.
25. Pulliam, T. H.; and Steger, J. L.: On Implicit Finite-Difference Simulations of Three-Dimensional Flow. AIAA Paper 78-10, 1978.
26. Steger, J. L.: Implicit Finite-Difference Simulation of Flow About Arbitrary Geometries with Applications to Airfoils. AIAA Paper 77-665, 1977.

27. Hsieh, T.: An Investigation of Separated Flow About a Hemisphere-Cylinder at 0- to 19-Deg Incidence in the Mach Number Range from 0.6 to 1.5. AEDC-TR-76-112, 1976.
28. Nietubicz, C. J.; Pulliam, T. H.; and Steger, J. L.: Numerical Solution of the Azimuthal-Invariant Thin-Layer Navier-Stokes Equations. AIAA Paper 79-0010, 1979.
29. McRae, D. S.: The Conically Symmetric Navier-Stokes Equations: Numerical Solution for Hypersonic Cone Flow at High Angle of Attack. AFFDL-TR-76-139, 1977.
30. Rainbird, W. J.: Turbulent Boundary-Layer Growth and Separation on a Yawed Cone. AIAA J., vol. 6, no. 12, 1968, pp. 2410-2416.

1. Report No. NASA TP-1749	2. Government Accession No.	3. Recipient's Catalog No.	
4. Title and Subtitle NUMERICAL SIMULATION OF STEADY SUPERSONIC VISCIOUS FLOW		5. Report Date May 1981	6. Performing Organization Code
		8. Performing Organization Report No. A-7923	10. Work Unit No. 505-31-41
7. Author(s) Lewis B. Schiff and Joseph L. Steger*	9. Performing Organization Name and Address Ames Research Center, NASA, Moffett Field, Calif. 94035		11. Contract or Grant No.
12. Sponsoring Agency Name and Address National Aeronautics and Space Administration Washington, D. C. 20546			13. Type of Report and Period Covered Technical Paper
15. Supplementary Notes *Present address: Dept. of Aeronautics and Astronautics, Stanford University, Stanford, Calif. 94305.		14. Sponsoring Agency Code	
		16. Abstract <p>A noniterative, implicit, space-marching, finite-difference algorithm is developed for the steady thin-layer Navier-Stokes equations in conservation-law form. The numerical algorithm is applicable to steady supersonic viscous flow over bodies of arbitrary shape. In addition, the same code can be used to compute supersonic inviscid flow or three-dimensional boundary layers. Computed results from two-dimensional and three-dimensional versions of the numerical algorithm are in good agreement with those obtained from more costly time-marching techniques.</p>	
17. Key Words (Suggested by Author(s)) Supersonic flow Navier-Stokes equations		18. Distribution Statement Unclassified - Unlimited Subject Category 02	
19. Security Classif. (of this report) Unclassified	20. Security Classif. (of this page) Unclassified	21. No. of Pages 42	22. Price* A03